The pristine Dwarf-Galaxy survey - V. The edges of the dwarf galaxy hercules

Nicolas Longeard, Pascale Jablonka, Giuseppina Battaglia, Khyati Malhan, Nicolas Martin, Rubén Sánchez-Janssen, Federico Sestito, Else Starkenburg, Kim A. Venn

Monthly Notices of the ROYAL ASTRONOMICAL SOCIETY

MNRAS **525,** 3086–3103 (2023) https://doi.org/10.1093/mnras/stad2227
Advance Access publication 2023 August 14

The Pristine dwarf galaxy survey–V. The edges of the dwarf galaxy Hercules

Nicolas Longeard,[1★] Pascale Jablonka,[1,2] Giuseppina Battaglia,[3,4] Khyati Malhan,[5] Nicolas Martin,[5,6] Rubén Sánchez-Janssen,[7] Federico Sestito,[8] Else Starkenburg[9] and Kim A. Venn[8]

[1]*Laboratoire d'astrophysique, École Polytechnique Fédérale de Lausanne (EPFL), Observatoire, CH-1290 Versoix, Switzerland*
[2]*GEPI, Observatoire de Paris, Université PSL, CNRS, Place Jules Janssen, F-92195 Meudon, France*
[3]*Instituto de Astrofísica de Canarias, E-38205 La Laguna, Tenerife, Spain*
[4]*Universidad de La Laguna, Dept. Astrofísica, E-38206 La Laguna, Tenerife, Spain*
[5]*Max-Planck-Institut für Astronomie, Königstuhl 17, D-69117 Heidelberg, Germany*
[6]*Observatoire astronomique de Strasbourg, Université de Strasbourg, CNRS, UMR 7550, F-67000 Strasbourg, France*
[7]*STFC UK Astronomy Technology Centre, Royal Observatory, Blackford Hill, Edinburgh EH9 3HJ, UK*
[8]*Department of Physics and Astronomy, University of Victoria, PO Box 3055, STN CSC, Victoria, BC V8W 3P6, Canada*
[9]*Kapteyn Astronomical Institute, University of Groningen, Landleven 12, 9747 AD Groningen, the Netherlands*

Accepted 2023 July 12. Received 2023 June 20; in original form 2023 April 25

ABSTRACT

We present a new spectroscopic study of 175 stars in the vicinity of the dwarf galaxy Hercules ($d \sim 132$ kpc) with data from the Anglo-Australian Telescope and its AAOmega spectrograph together with the Two Degree Field multi-object system to solve the conundrum that whether Hercules is tidally disrupting. We combine broad-band photometry, proper motions from *Gaia*, and our Pristine narrow-band and metallicity-sensitive photometry to efficiently weed out the Milky Way contamination. Such cleaning is particularly critical in this kinematic regime, as both the transverse and heliocentric velocities of Milky Way populations overlap with Hercules. Thanks to this method, three new member stars are identified, including one at almost $10r_{\rm h}$ of the satellite. All three have velocities and metallicities consistent with that of the main body. Combining this new data set with the entire literature cleaned out from contamination shows that Hercules does not exhibit a velocity gradient ($\mathrm{d}\langle v\rangle/\mathrm{d}\chi = 0.1^{+0.4}_{-0.2}$ km s^{-1} arcmin^{-1}, 1.6 km s^{-1} arcmin^{-1} as a 3σ upper limit) and, as such, does not show evidence to undergo tidal disruption.

Key words: galaxies: dwarf – Local Group.

1 INTRODUCTION

Companion galaxies orbiting the Milky Way (MW) have been discovered at an incredible rate over the last few years, under the impulsion of various photometric surveys that are ideal to detect faint surface brightness systems (Sloan Digital Sky Survey, SDSS, York et al. 2000; the Panoramic Survey Telescope And Rapid Response System, PS1, Chambers et al. 2016; the Dark Energy Survey, The Dark Energy Survey Collaboration 2005). The faintest of them are commonly referred to as ultra-faint dwarf galaxies (UFDs).

Intensive spectroscopic observations of these very faint systems followed, mainly focusing on their dynamical and metallicity properties (e.g., Simon & Geha 2007; Martin et al. 2007; Koposov et al. 2011; Walker et al. 2016; Kirby et al. 2017; Fritz et al. 2019; Chiti et al. 2022). Associated with photometric properties, these chemo-dynamical observations are instrumental to our understanding of both the nature of dark matter and the physical processes governing the evolution of baryons. These extensive observations uncovered discrepancies with respect to hydro-dynamical simulations that are yet to be solved. A first example is the diversity of rotation curves that show that the slope of the dark matter inner density density profile is shallower than expected (Flores & Primack 1994; Moore 1994; Oman et al. 2015). Furthermore, it is challenging for simulations to properly reproduce the metallicity–luminosity relation (Simon & Geha 2007; Kirby et al. 2013; Sanati et al. 2023) showing that the predicted star-formation histories and/or stellar yields for the UFDs are not correct, or that the observations are still incomplete and that specific efforts should be put on that front. A final, well-known example is the plane of satellites observed in several galaxy groups (Lynden-Bell 1976; Kunkel & Demers 1976; Pawlowski et al. 2022) stating that the existence of a rotationally supported, thin polar structure around galaxies such as the MW is extremely improbable, therefore questioning the validity of the current standard cosmological model. These issues will only be solved through a careful analysis of the properties of the faintest satellite galaxies of the MW.

However, as more and more UFD member stars are studied, a new light has been recently shed on the faintest satellites, that focus on their potential stellar haloes. If this component is highly hypothetical at such low mass, especially since their existence may relate to early mergers (Chiti et al. 2021; Tarumi, Yoshida & Frebel 2021) that are less common as one goes down the mass scale of galaxies (Deason et al. 2022). Of course, the observationability of these haloes, should they exist in a given system that is already low surface brightness,

★ E-mail: nicolas.longeard@epfl.ch

Table 1. Summary of Hercules' property. The references number correspond to the following list: (1) Muñoz et al. (2018), (2) Simon & Geha (2007), (3) Adén et al. (2009b), (4) Deason et al. (2012), and (5) Gregory et al. (2020).

Property	Inference	Reference
d_{GC} (kpc)	132.0 ± 6.0	(1)
r_h (arcmin)	5.83 ± 0.65	(1)
r_h (pc)	216 ± 20	(1)
$\langle v \rangle$ (km s^{-1})	45.0 ± 1.1	(2), (3), (4), (5)
[Fe/H]	-2.39 ± 0.04	(2), (3), (4), (5)

makes their detection extremely difficult, even if recent studies have started to put them in evidence in several galaxies (Johnson et al. 2020; Pace et al. 2020; Chiti et al. 2021; Longeard et al. 2022; Qi et al. 2022). Jensen et al. (prep.) also report a few dwarf galaxies of the MW, among the 60 that went under scrutiny, for which the existence of an extended stellar halo is credible.

These efforts reveal additional layers of complexity in the kinematics and metallicity properties of the faintest galaxies. Two recent examples illustrate this complexity. The first one concerns the faint Tucana II (Tuc II, $d \sim 58$ kpc) satellite galaxy (Chiti et al. 2021). Their seven member stars located at galactocentric distances between 2 and 9 times the Tuc II's half-light radius (r_h) tend to be more metal-poor than those in the galaxy central region. Should this metallicity trend be found in other UFDs, it would mean that our current view of the metallicity distribution functions (MDF) of these systems are biased, and might be lower. This would have strong implications on the galaxy formation simulations that are fine-tuned to reproduce the observed metallicities (see Sanati et al. 2023 for further discussion). The second striking example of rising complexity in UFDs is the case of Bo'otes I (Boo I, $d \sim 66$ kpc). Longeard et al. (2022) identified 17 members in the outskirts of the satellite, including one at $\sim$4.1 r_h. They measured both negative metallicity and velocity gradients in the system. These results show that our current view of the mass functions of UFDs can also be significantly biased towards higher values, since the introduction of a velocity gradient in Boo I dynamical modelling deflates its dynamical mass by $\sim$40 per cent with respect to a simpler model with a constant systemic velocity, that is, if the assumptions underlying its computation still hold (Wolf et al. 2010). These two recent examples perfectly illustrate the need for more spectroscopic observations in the outskirts of UFDs. If the hope for studying dwarf galaxies's halo as a whole component is extremely thin due to their predicted low surface brightness from simulations (Deason et al. 2022), it is still possible to detect a few large galactocentric distance stars (Yang et al. 2022 for Fornax; Sestito et al. 2023a, b for Sculptor and Ursa Minor; Waller et al. 2023 for Coma Berenices, Ursa Major I and Bo'otes I). In particular, the work of Waller et al. (2023) focused on high-resolution spectroscopy, and abundance derivation of the outskirts of these three galaxies suggest that at least some of the stellar population of these haloes can form in the inner region and migrate during the dwarf's history, while confirming that minor mergers are viable pathways to form dwarf galaxy's haloes in the case of Bo'otes I.

In this work, we propose to follow-up on that effort to study Hercules, a dwarf galaxy that has been the subject of speculation regarding its potential tidal disruption status. Its main properties are summarized in Table 1. This question can only be answered through the search for extra-tidal stars at large galactocentric distances that offer the largest velocity contrast with the main body. The large ellipticity and tentative velocity gradient of Hercules (Adén et al. 2009a; Martin & Jin 2010) have warranted speculation. So far the vast majority of Hercules' known members are located in the galaxy central region. Part of this spatial limitation is due to the fact that their identification is easier with such an observational strategy, but also because its systemic heliocentric velocity and proper motion (PM) are blended into the MW's. Therefore, the identification of new members is extremely challenging. Finding those with high confidence at large distances from the kinematic information alone is almost an impossible task.

Aside from the identification of new member stars, one element has been the centre of discussion: does Hercules possess a velocity gradient that would be the telltale sign of an undergoing tidal disruption? Adén et al. (2009b) were the first one to detect such a gradient with their significant spectroscopic sample of 28 red giant branch (RGB) member stars, with $\mathrm{d}\langle v \rangle / \mathrm{d}\chi = 16 \pm 3$ km s^{-1} kpc^{-1}. They immediately associated this detection with tidal disturbances in the outskirts of the UFD. Martin & Jin (2010)'s results were in line with this initial study. However, Deason et al. (2012) did not detect any gradient, though they make it clear that their low velocity precision, due to the poor resolution of the spectrograph used ($R \sim 2000$), may be the reason behind this non-detection. The sections 3.1.2 and 3.1.3 of Gregory et al. (2020) offer detailed analyses on Hercules' velocity gradient under different assumptions. First, using only their own new nine members and with a uniform prior on the galaxy position angle, they did not detect any dependence of the velocity with distance. However, assuming that Hercules' velocity gradient runs along its major axis at a position angle of -78 deg, as detailed by Martin & Jin (2010), they did find a gradient of $9.4^{+6.0}_{-6.3}$ km s^{-1} kpc^{-1}. Combining these results with the spectroscopic sample of Simon & Geha (2007) yielded a similar result. Finally, Küpper et al. (2017) and Fu, Simon & Alarcón Jara (2019) pointed out that their predicted velocity gradients for Hercules, based on *N*-body simulations of the UFD, are inconsistent with the one found by Adén et al. (2009b), and should be much lower, of 4.9 and 0.6 km s^{-1} kpc^{-1}, respectively.

Furthermore, Garling et al. (2018) recently identified three new RR lyrae stars in Hercules outside the estimated tidal radius of Hercules, adding to the previously nine RR Lyrae identified prior to their study (Musella et al. 2012). They interpreted their results as proof that some Hercules stellar material have been stripped from the system. Interestingly enough, one of their three new finding is not aligned with the major axis of the system, but with its minor axis.

More recently, Errani et al. (2022) shows that Hercules's velocity dispersion and size should have been affected by tides, according to their set of *N*-body simulations, actually lying very close to their tidal track limit (i.e. the maximum size reachable by a dwarf galaxy given its circular velocity).

The following list: Adén et al. (2009b), Martin & Jin (2010), Simon & Geha (2007), Deason et al. (2012), Fu et al. (2019), and Gregory et al. (2020) are the papers that will be referred to as 'the literature' in the rest of this work.

The case of Hercules therefore remains open, as even the existence of a velocity gradient is still not clear, nor is its expected value should it exist. We therefore try to solve this conundrum with a re-analysis of the kinematic and metallicity properties of Hercules, using new spectroscopic observations at large galactocentric distances combined with the entire literature that include spectroscopic data.

2 SPECTROSCOPIC OBSERVATIONS

This section provide details on the target selection, observations and data reduction. It also introduces our pipeline to derive heliocentric velocities and equivalent widths from the spectra.

2.1 Data selection and acquisition

An overview of all our new targets is shown in Fig. 1. The coordinates used throughout this work are found from our photometric reduction pipeline of the Pristine field, which is calibrated according to the *Gaia* astrometry. We also show the colour–magnitude diagram (CMD) in the right-hand panel, using SDSS magnitudes. This spectroscopic sample was obtained on the Anglo-Australian Telescope (AAT; Lewis et al. 2002) and its Two Degree Field (2dF) multi-object system (Cannon 1997) through the OPTICON program. The gratings used were 580 V for low-resolution spectra in the optical ($R \sim 1300$, 3700–5500Å), and 1700D for calcium triplet spectra with a spectral resolution R of ∼11 000. Only the red part of the spectra (from 8400 to 8800 Å) is used for the rest of this work. The observations were carried out on 2022 May 02 and 03. One more night was scheduled but lost due to bad weather. The 2dF spectrograph possesses ∼360 science and ∼40 sky and guiding fibers. During the first night, both fields benefitted from four sub-exposures of 2400 s each. However, on the second night, only two out of the four sub-exposures were observed for Field 2. As a consequence, Field 2 spectra for the second night are non-exploitable, and only the ones from the first night are considered. For Field 1, the final spectra are obtained by coadding the first and second nights. The total exposure time is 19 200s for Field 1 and 9600s for Field 2. Spectra were gathered for 295 stars.

The two fields were placed at each extremity of the UFD along its major axis in order to find potential tidal tails. These two fields are shown in Fig. 1 and extend as far as ∼13 half-light radii (r_h) of Hercules. All targets were selected based on the Pristine survey data (Starkenburg et al. 2017). Pristine is a photometric survey relying on a narrow-band, metallicity-sensitive photometry centred on the Calcium H&K doublet lines taken on the Canadian France Hawaii Telescope (CFHT; Boulade et al. 2003). It is successful at finding metal-poor stars against the more metal-rich MW contamination (Youakim et al. 2017; Aguado et al. 2019; Arentsen et al. 2020) and is therefore particularly suited for the UFDs metal-poor population (Longeard et al. 2020; 2021; 2022). For Hercules, this photometry is based on two components:

(i) A mosaic of deep Pristine images centred on Hercules, shown in Fig. 1, yielding reliable photometric metallicities down to $g_0^{\rm SDSS} \sim 22.5$.
(ii) Shallower photometry corresponding to the Pristine main survey covering the far outskirts of the satellite, yielding reliable photometric metallicities down to $g_0^{\rm SDSS} \sim 21.5$

As illustrated in Fig. 1, most of our targets were selected from the deep photometry region. Three main criteria were applied to select them:

(i) Stars located further than 0.3 mag from the best-matching Hercules isochrone ($A = 12$ Gyr, [Fe/H] $= -2.0$, [α/Fe] $= 0.0$, $m - M = 20.68$) from the Darmouth library (Dotter et al. 2008) were discarded.
(ii) The photometric metallicity of all targets should be lower than −0.5.
(iii) The proper motion membership probability of all targets must be of at least 1 per cent, based on the *Gaia* Data Release 3 (Gaia Collaboration 2022). These membership probabilities are computed assuming two multivariate Gaussian populations in proper motion space, for Hercules and the MW, respectively. Our final systemic proper motion ($\langle \mu_\alpha^* \rangle = -0.037 \pm 0.029$ mas yr^{-1}, $\langle \mu_\delta \rangle = -0.365 \pm 0.043$ mas yr^{-1}) for the UFD is compatible with the ones of Battaglia et al. (2022) and McConnachie & Venn (2020).

These constraints are loose because of the large number of fibers available in the spectrograph. Even then, a significant fraction of fibers were still unassigned and therefore filled even lower priority stars and interesting, potentially extremely metal-poor ([Fe/H] <-3.0) MW halo stars according to Pristine.

2.2 Data reduction

The AAT 2DFDR[1] package and the standard settings were used to reduce the spectra, with two small exceptions detailed in the 'Data Reduction' section of Arentsen et al. (2020) regarding the coadding of multiple spectra. The first one is that the weight attributed to each exposure is now determined by object and not by frame, while the second exception is to turn off the ADJUST_CONTINUUM parameter that can produce unphysical CaT line shapes.

Three examples of spectra for low (6.7), mid (14.4), and high (30.7) signal-to-noise (S/N) ratios are shown in Fig. 2. As shown by this plot, the observing run suffered from an extremely large sky contribution in each spectrum, especially in the vicinity of the third CaT line, which causes the fitting of this line to be challenging, even for high S/N, although not impossible as a minority of spectra have a prominent enough third line. Extensive testing of different sky subtraction methods, internal and external to the AAT 2DFDR software, led to the conclusion that the issue does not lie with the sky subtraction itself, which is conducted properly by the software, but by the fact that the sky contributions can be so large that even small residuals remain significant with respect to the stellar spectra. Each spectrum was therefore carefully visually inspected and discarded if its quality was too poor to obtain a proper fit of any of the three CaT lines, i.e. that the code is actually fitting noise. This step led to the rejection of 145 spectra, i.e. almost 50 per cent of our sample. Among those, ∼23 stars were high-probability member candidates. A histogram of the g_0 magnitude of good versus rejected spectra is shown in Fig. 3, illustrating that this quality cut is made at the expense of going deeper into the RGB of Hercules.

The spectra are normalized by finding the continuum following the method of Battaglia et al. (2008b), i.e. through an iterative k-sigma clipping non-linear filter. The heliocentric velocities and equivalent widths (EWs) of each spectrum is then obtained using our in-house pipeline described in detail in Longeard et al. (2022), that has already been extensively tested against known metallicities and velocities. Each CaT line is modelled with a Gaussian and Voigt profile and their position are found by minimizing the squared difference between a synthetic spectrum composed of three Gaussian/Voigt profiles and the observed spectrum. The EWs are calculated by integrating the best fit around each line in a 15 Å window. This is performed with a Monte Carlo Markov Chain (MCMC; Hastings 1970) algorithm with a million iterations per spectrum. The median of the velocity uncertainty is 7.5 km s^{-1} for the new AAT sample, 4.0 km s^{-1} for entire sample (literature + AAT, details in Section 3.2), and 3.3 km s^{-1} when the sample is restricted to Hercules member stars only.

3 RESULTS

We present in this section the results of our spectroscopic analysis, both dynamical and in terms of metallicity. We start with the

[1] https://aat.anu.edu.au/science/software/2dfdr

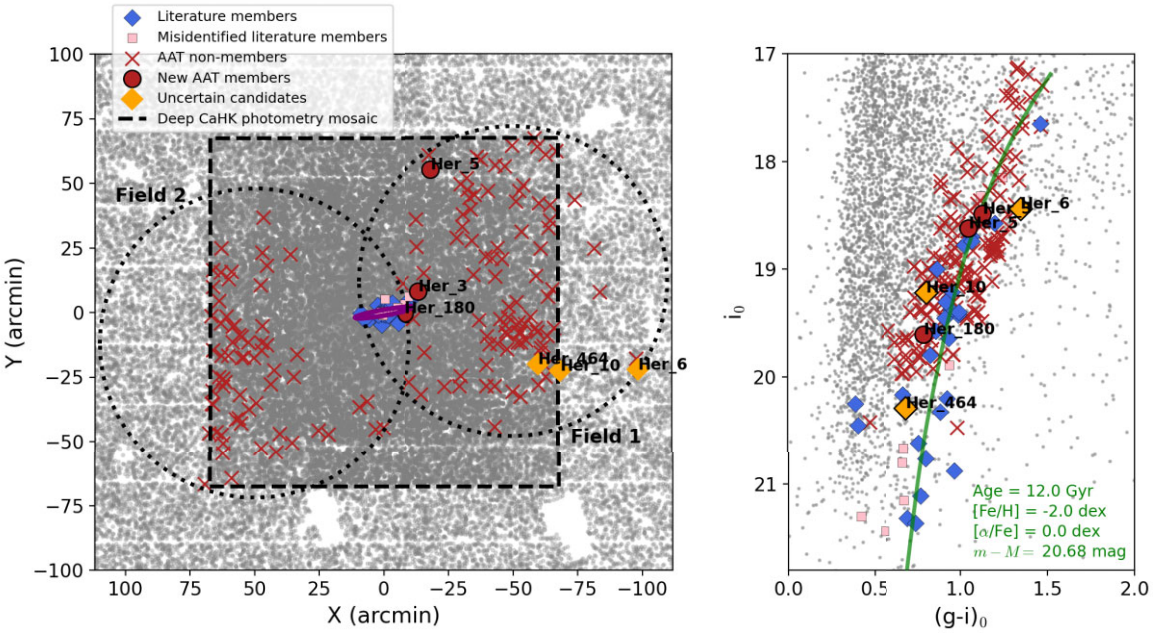

Figure 1. Left-hand panel: spatial distribution of the AAT spectroscopic sample. Newly discovered members are shown as red circles, while uncertain candidates are shown as orange diamonds. Non-members from the AAT sample are shown as red crosses. Previously known members from the literature are represented as smaller blue diamonds. Misidentified literature members are shown as small pink squares. The two half-light radii of Hercules as inferred by Muñoz et al. (2018, M18) are shown as a purple ellipse. Right-hand panel: CMD of our spectroscopic sample superimposed with a metal-poor Darmouth isochrone at the distance of Hercules. The *g* and *i* magnitudes are from SDSS.

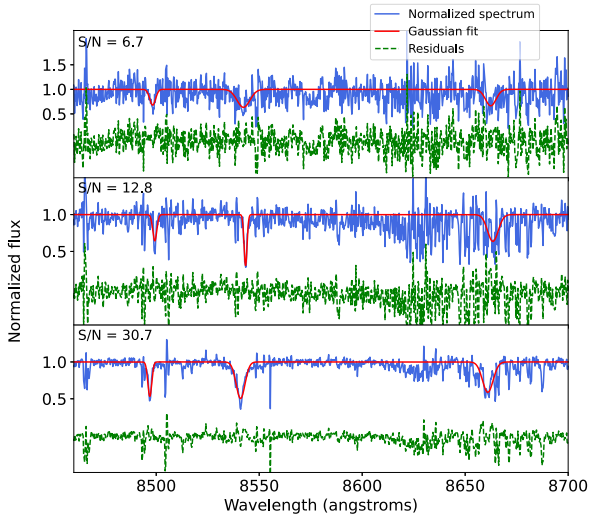

Figure 2. Example spectra of three stars in our AAT data set centred on the calcium triplet lines. Due to the low number of new members identified, only one spectrum displayed here is a Hercules members, i.e. the second one. This spectrum is however representative of the quality of the Her' members. Each star represents respectively the low, mid, and high S/N regimes. The normalized spectra are shown with solid blue lines while the fits derived from our pipeline for Gaussian profiles are shown with solid red lines. Residuals in the Gaussian cases are shown for each case below the spectra as green dashed lines. While the two first lines are properly fitted, the large sky residuals are often too large to fit the third CaT line, even for the high signal-to-noise ratio (SNR) regime. These stars have a heliocentric velocity of 31.9 ± 3.2, 45.5 ± 1.4, and −39.9 ± 1.1 km s^{-1} from top to bottom.

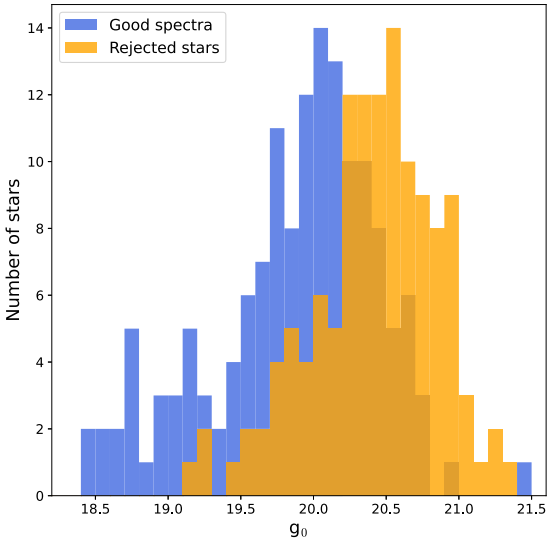

Figure 3. Histogram of the dust-corrected, SDSS g magnitude for all stars with an SNR >= 3 with good (blue) and poor (orange) quality spectra. Our final sample is composed of the 175 stars in the blue sample, while the rest is rejected.

metallicity results since it is the most discriminative property between Hercules's stellar population and the MW's.

3.1 Metallicity properties

The stellar velocity distribution of Hercules overlaps with that of the MW (see Section 3.2 for more details). Therefore, MW stars can easily be misidentified as Hercules members from a purely dynamical standpoint. An additional selection is needed. Fig. 4 shows the MDFs of the MW in the direction of Hercules as predicted by the *Gaia* Universe Model Snapshot (GUMS; Robin et al. 2012). We superimpose the spectroscopically confirmed Hercules members

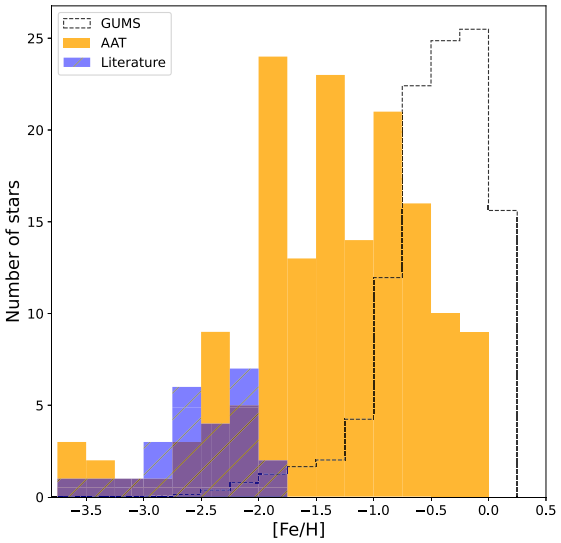

Figure 4. MDFs of the MW contamination as predicted by GUMS (dotted black), the full AAT sample (plain orange), and the literature (dashed blue). The AAT MDF is calculated with both spectroscopic and photometric metallicities from the Pristine survey. The mean metallicity of the AAT sample is naturally lower than the one of GUMS as a Pristine pre-selection on the metallicity was applied prior to observation.

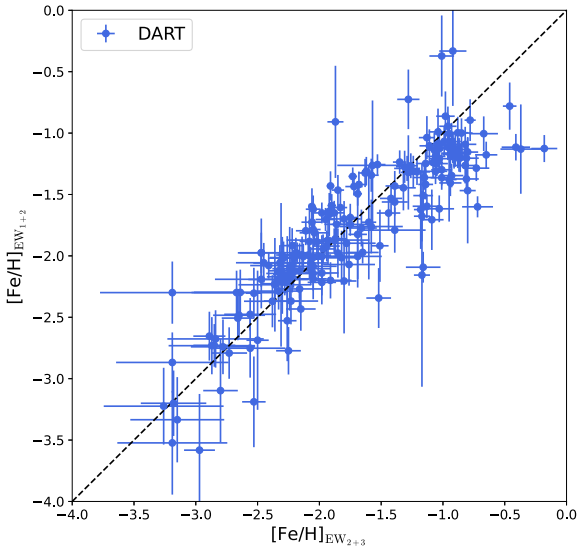

Figure 5. Comparison between metallicities obtained from the calibration of Carrera et al. (2013) using the second and third CaT lines (x-axis) and ours based on the first two lines (y-axis) for DART (blue). The 1:1 line is shown with the black dashed line.

from the literature. While all Hercules' stars have a spectroscopic metallicity below −1.5, the MW population is mostly more metal-rich, with only the tail of the [Fe/H] distribution intersecting with that of the MW. Therefore, the metallicity is an appropriate way of discriminating the two populations.

However, spectroscopic metallicities derived from the CaT lines require clean spectra with an S/N of 10 at the very least. As mentioned in Section 2.2, this is not the case for most of our spectra, that not only have a lower S/N, but also are polluted with sky residuals. Moreover, the classical CaT calibrations rely on the second and third lines, since the first one typically has a lower S/N than the other two (Starkenburg et al. 2010; Carrera et al. 2013).

A total of 29 stars have spectra with SNR >10. We can properly fit the third line of the CaT for eight of them. For these, we can therefore use the empirical calibration of Carrera et al. (2013). Their uncertainties are derived by performing a 10 000 iterations Monte Carlo sampling on all the parameters involved in the calibration, i.e. the V absolute magnitude, the distance modulus of Hercules, the EWs, and the calibration coefficients.

In order to derive the CaT metallicities of the 21 remaining high SNR AAT stars, we derive a new empirical calibration based only on the two first lines based on a sample of 220 RGB stars with S/N of 10 or higher from the *dwarf galaxy abundances and radial-velocities team* (DART; Tolstoy et al. 2004; Battaglia et al. 2006; Tolstoy et al. 2006; Battaglia et al. 2008a, 2011) belonging to the Fornax, Sextans, and Sculptor Dwarf Spheroidals. The same formalism as Starkenburg et al. (2010) and Carrera et al. (2013) is used, i.e.:

$$[\mathrm{Fe/H}]_{1+2} = a + b \times V + c \times \mathrm{EW}_{1+2} + d \times \mathrm{EW}_{1+2}^{-1.5} + e \times \mathrm{EW}_{1+2} \times V \quad (1)$$

with a, b, c, d, and e the new calibration coefficients, EW_{1+2} the sum of the first and second CaT lines equivalent widths assuming a Voigt profile, and V the V absolute magnitude of the star. Our pipeline is used to derive the EWs of the first two lines of the DART stars. The coefficients are then found by a least square minimization with respect to the 'true' metallicities given by the DART papers, through an MCMC algorithm. The resulting coefficients are reported in Table 1. Note that these coefficients are highly correlated and cannot, as face value, be used to determine a metallicity unless one uses the full MCMC chains to draw the coefficients from. Fig. 5 shows that the two calibrations are in excellent agreement. Similarly, for the eight stars for which the EW of the third line can be properly measured, both calibrations are also compatible with each other. For homogeneity purposes, even for these eight stars, we use the metallicity obtained from our new calibration.

At this stage, all 29 AAT stars with an S/N >10 have a potential spectroscopic metallicity measurement. However, these CaT calibrations hold only if a star is a Hercules member, since their distance is considered when computing the spectroscopic metallicities. In order to have a metallicity estimate, irrespective of the SNR of their spectra or membership status, we also assign a Pristine metallicity estimate to the full sample. The final AAT MDF, composed of both spectroscopic metallicities (when possible) and photometric metallicities otherwise is shown in orange in Fig. 4. The next step is to use the discriminative power of Hercules' metallicity to accurately derive its kinematic properties.

3.2 Dynamical analysis

The velocities of the new AAT sample are obtained using the pipeline described in Section 2.2. For our observational set-up, Li et al. (2019) show that both a velocity offset and a velocity uncertainty corrections are needed. The offset is of the order of 1.1 km s^{-1}, while the uncertainties are corrected using the following relation:

$$\delta_v = \sqrt{(1.28\delta_v^{\mathrm{fit}})^2 + 0.66^2},$$

with δ_v^{fit} the intrinsic velocity uncertainty derived by the CaT lines fit. The velocity measurements reported in Table 2 include these corrections.

The heliocentric velocity distributions of the new AAT sample alone and combined with the literature values are shown in Fig. 6. As shown by the top panel, the case of Hercules is challenging

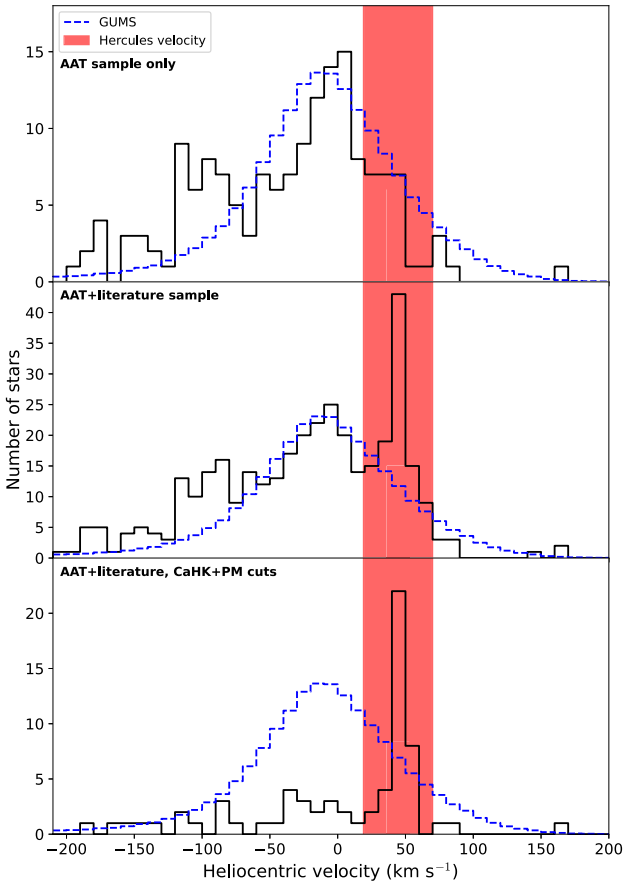

Figure 6. Top panel: velocity histogram for the new AAT sample. The blue dashed histogram corresponds to the GUMS velocities in the region of Hercules. The red transparent rectangle shows the 3σ interval of Hercules' dynamical population. Middle panel: velocity histogram of the AAT sample combined with the literature. Bottom panel: Final velocity distribution, when the AAT + literature sample is cleaned based on the photometric and *Gaia* criteria detailed in Section 3.2.

as its velocity distribution is enclosed in the predicted MW stars' line-of-sight velocity in that region of the sky, according to GUMS. Taken alone, our AAT sample does not exhibit any velocity peak. We therefore combine the AAT data set with previous spectroscopic studies over the years: Adén et al. (2009a), Martin & Jin (2010), Deason et al. (2012), Fu et al. (2019), and Gregory et al. (2020). The resulting sample is shown in the middle panel of Fig. 6.

From this sample composed of the new AAT spectroscopy and the literature combined (368 stars in total), we reduce the potential contamination of the MW which could bias our result. To this end, we take into account the photometric (broad-band and *CaHK*) and *Gaia* (see $\mathcal{L}_{\rm PM}^{\rm Her}$, equation 2) information of each star. All these properties are combined in the final likelihood equation (see equation 3) to derive the dynamical properties. For clarity, we first derive each of these likelihoods and photometric criteria separately, before combining them all to produce the final sample.

3.2.1 *The broad-band and* CaHK *photometry information*

The initial sample is composed of 368 stars. From those, 162 have a SNR above 3 and a velocity uncertainty below 15 km s $^{-1}$ .The properties of these stars are shown in Table 3.

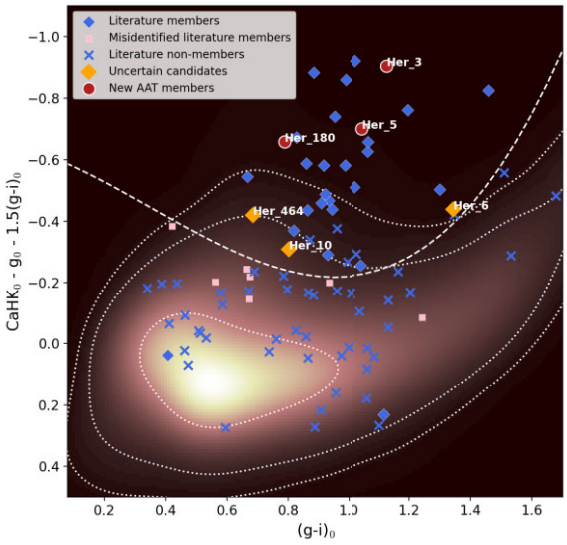

Figure 7. Pristine colour–colour space, with the $(g-i)_0$ temperature proxy and the $\mathrm{CaHK}_0 - g_0 - 1.5(g-i)_0$ colour on the y-axis. In this plot, [Fe/H] decreases as values on the y-axis decrease. The density plot of the MW contamination is also shown with the colour scale. The density decreases as the colour goes darker. The 1, 2, and 3σ contours are shown as white dotted lines. Literature members and non-members are shown as blue diamonds and crosses, respectively and are only the ones with a spectroscopic metallicity and a proper motion measurement to ensure their membership status. Our new AAT members as shown as red circles, while uncertain candidates are represented as orange diamonds. Misidentified literature members are represented by small pink squares.

From the initial 368 stars, the ones with a membership probability based on their location on the Hercules CMD lower than 10 per cent (these probabilities are computed following the same method detailed by Longeard et al. 2018) are discarded. This leads to the exclusion of 122 stars.

Then, a photometric metallicity cut using the CaHK photometry is applied. However, rather than using a single metallicity value as a threshold to determine the final sample, this criterion is built in the Pristine colour–colour space shown in Fig. 7. In order to estimate the stellar density of the MW, we bin all stars with distances from the centre of Hercules larger than $5r_{\rm h}$. The resulting grid is then convolved with a 0.1 mag 2D Gaussian kernel on each axis. We then superimpose the literature spectroscopic and PM confirmed members and non-members. In this colour–colour space that is metallicity-sensitive (with metallicity decreasing as one goes upwards in the diagram), there is a clear dichotomy between the Hercules members and non-members, the former being more metal-poor than the MW stars. We therefore trace a line separating the two populations shown as the dashed white one in Fig. 7. The final sample, on which the dynamical properties will be derived, is composed solely of stars located in the region above that line. In doing so, we take the risk of missing some metal-rich Hercules members located in the discarded area. However, this risk should be extremely low as most of our targets are located in the outskirts of the galaxy which are expected to have a lower metallicity than that of the main body. This is true even for UFDs, as demonstrated recently by Chiti et al. (2021) for Tucana II and by Longeard et al. (2022) for Bootes I. This cut further excludes 157 stars.

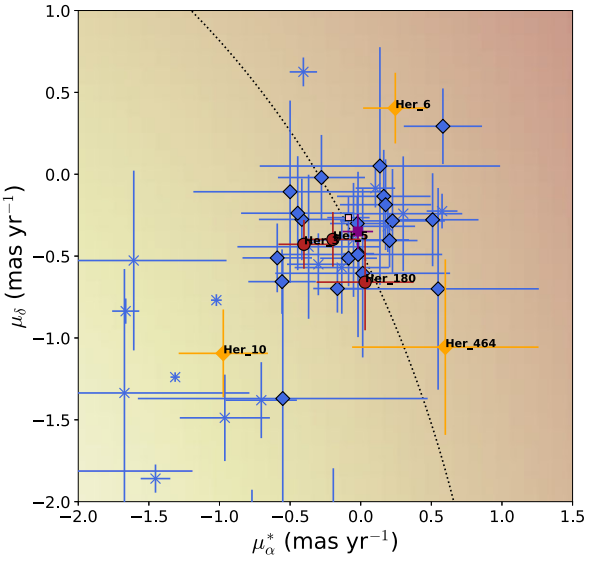

Figure 8. PM space showing the confirmed literature members as blue diamonds, literature non-members as blue crosses, and all new AAT members as red circles. Uncertain candidates are represented by orange diamonds. Misidentified literature members are represented by small pink squares. The large purple square shows the systemic PM of Hercules as derived in this work, compatible with the ones of Battaglia et al. (2022) and McConnachie & Venn (2020). The underlying distribution represents the MW population in that region of the sky, assuming it can be modelled as a multivariate Gaussian. The dashed black line corresponds to the 1σ contour of this MW population.

3.2.2 *The Gaia information*

We now have a sample composed of 89 stars. We now apply an effective temperature and parallax cut: every star with $T_{\rm eff} > 5800$ K and Plx/e_plx > 2.0 are discarded, with $T_{\rm eff}$ the effective temperature measured by *Gaia* DR3, Plx the parallax, and e_plx its corresponding uncertainty. These criteria discard 13 stars.

The PM information is then folded in by estimating the local MW contamination in PM space assuming a 2D Gaussian mixture models to the PM distribution shown in Fig. 8. This step corresponds to the likelihood:

$$\mathcal{L}^{\rm Her}_{\rm PM}(\mu^*_{\alpha,k}, \mu_{\delta,k}, d\mu^*_{\alpha,k}, d\mu_{\delta,k}|\langle\mu^*_\alpha\rangle, \langle\mu_\delta\rangle, \sigma_\alpha, \sigma_\delta, c) = \mathcal{G}_{2D}(\mu^*_{\alpha,k}, \mu_{\delta,k}, d\mu^*_{\alpha,k}, d\mu_{\delta,k}|\langle\mu^*_\alpha\rangle, \langle\mu_\delta\rangle, \sigma_\alpha, \sigma_\delta, c)) \quad (2)$$

with $\langle\mu^*\rangle$ and σ the systemic proper motion and proper motion dispersion, c the correlation and μ^*_k the individual PM measurement. The '$\mathcal{G}_{2D}$' notation stands for a 2D Gaussian function. This equation is only shown as a functional form and can also be applied to the MW. This step is then folded in the final likelihood detailed in equation (3). It is not a dichotomic cut, i.e. stars are not discarded of the sample altogether based on their PM measurements, but their PM membership probability following equation (2) will intervene in the kinematic properties derivation, through equation (3) detailed later. For stars without a PM measurement, we set their PM to be 0 mas yr^{-1} and their PM uncertainty to be 10^6 mas yr^{-1}.

From the photometric cuts and the PM information, a total of 11 literature members are found not to be members of Hercules. Their properties are detailed in Table 4, with the last column indicating the main information used to make the decision. In particular, it is interesting to note that the two most metal-rich literature members belong to this misidentified member sample, since their PM is largely discrepant from that of Hercules.

Table 2. New calibration coefficients.

Coefficient	Inference
a	-1.380 ± 0.720
b	0.290 ± 0.280
c	0.024 ± 0.200
d	-3.890 ± 0.980
e	-0.097 ± 0.790

3.2.3 *The kinematic analysis*

At this stage, the remaining sample is composed of 76 stars, both from the literature and the new AAT spectroscopic sample.

The final step before inferring Hercules' new dynamical properties is to properly handle the potential velocity offsets between the different spectroscopic data sets. They are indeed observed at different times with different set-ups, which can introduce velocity offsets between different data sets that need to be corrected for. Ideally, using the formalism of Minor et al. (2019) that proposes to add as many unknown offset parameters to infer as there are different spectroscopic set-ups to find the systematic differences between them would be sufficient. However, this method fails for small data sets and/or when the UFD's population is blended with that of the MW. For Adén et al. (2009a) and Gregory et al. (2020), a cross-match is therefore performed between each data set and the reference one of Simon & Geha (2007). The offset is then derived through an MCMC procedure, and, during the dynamical analysis, we randomly draw into the posterior probability distribution function (PDF) to account for the uncertainty of each offset. The resulting offsets are respectively of -0.8 ± 3.5 and 3.0 ± 5.0 km s^{-1}.

Finally, for Deason et al. (2012), the same method is applied but in two steps: the offset between this catalogue and the one of Adén et al. (2009a) is found. Then, we apply a second offset between the latter and the Simon & Geha (2007) data set. The reason for this intermediate step is that the cross-match between the data sets of Deason et al. (2012) and Adén et al. (2009a) yields more stars in common than directly cross-matching with Simon & Geha (2007), therefore constraining better the offset. The resulting offset is of -10.2 km s^{-1}.

Finally, for our AAT sample, the offset is also found in two steps. First, the one from Longeard et al. (2022) between the set-up used in this work and the Keck/DEIMOS set-up in the red, of 7.2 ± 1.6 km s^{-1}, used by Martin et al. (2007), is considered. This DEIMOS set-up is the same as the one used by the reference sample of Simon & Geha (2007), and should therefore apply in our case. Then, using the cross-match of the data sets of Simon & Geha (2007) and Martin et al. (2007) for three other dwarf galaxies, we find a systematic of 2.7 ± 1.8 km s^{-1}, which is added to the one of Longeard et al. (2022) to give the final offset between these two set-ups. To summarize, we combine the velocity offset between Longeard et al. (2022) and Martin et al. (2007) and the one between Martin et al. (2007) and Simon & Geha (2007), to obtain the final offset between this work and Simon & Geha (2007). The velocity difference of the star in common between the reference data set and the AAT sample, of $\sim$8 km s^{-1}, supports this choice. Fig. 9 presents the velocity differences between the different spectroscopic samples.

The dynamical properties of Hercules are derived following the formalism of Martin & Jin (2010) combined with the likelihoods

Table 3. Properties of the new AAT spectroscopic sample. The individual spectroscopic metallicities for our calibration (i.e. using CaT lines 1+2) are reported for member stars with S/N ≥10. Confirmed new members are denoted with 'Y' in the member column, while uncertain candidates according to the definition in Section 3.2.3 are denoted with '?'.

RA (deg)	DEC (deg)	$g_0^{\rm SDSS}$	$i_0^{\rm SDSS}$	CaHK$_0$	$v_{\rm r}$ (km s^{-1})	μ_α^* (mas yr^{-1})	μ_δ (mas yr^{-1})	S/N	[Fe/H]$_{1+2}^{\rm spectro}$	[Fe/H]$_{\rm Pristine}$	Member
246.87308	13.56735	19.47 ± 0.02	18.36 ± 0.01	21.05 ± 0.08	−80.1 ± 4.2	−0.18 ± 0.18	−0.27 ± 0.15	14.4	—	−0.57	N
246.60181	12.40716	20.02 ± 0.02	19.22 ± 0.02	20.91 ± 0.08	−51.7 ± 11.5	−0.97 ± 0.32	−1.09 ± 0.27	3.0	—	−1.67	?
248.81762	12.76141	19.29 ± 0.02	18.33 ± 0.01	20.51 ± 0.06	−87.7 ± 4.2	−3.86 ± 0.14	−6.46 ± 0.12	13.1	—	−1.11	N
248.78361	13.04866	19.93 ± 0.02	18.75 ± 0.02	21.47 ± 0.12	24.9 ± 9.1	−1.54 ± 0.22	−4.12 ± 0.18	5.3	—	−0.80	N
247.55662	13.38471	19.76 ± 0.02	18.49 ± 0.01	21.32 ± 0.10	43.2 ± 5.8	2.15 ± 0.16	−13.18 ± 0.13	12.4	—	−1.20	N
248.80239	13.00075	18.93 ± 0.01	17.77 ± 0.01	20.42 ± 0.07	1.3 ± 4.0	−0.08 ± 0.10	0.15 ± 0.09	11.4	—	−0.83	N
246.69826	12.36966	20.32 ± 0.03	19.63 ± 0.02	21.09 ± 0.10	9.8 ± 9.9	−0.61 ± 0.47	−1.67 ± 0.39	4.4	—	−1.74	N
247.50016	12.52366	20.48 ± 0.03	19.80 ± 0.03	21.41 ± 0.12	−197.4 ± 10.1	−0.62 ± 0.42	−1.60 ± 0.35	3.7	—	−0.99	N
247.50492	13.03883	20.30 ± 0.03	19.68 ± 0.03	20.75 ± 0.07	−79.8 ± 10.8	−1.50 ± 0.41	−0.95 ± 0.34	6.2	—	−3.36	N
247.65178	12.9711	20.35 ± 0.03	19.24 ± 0.02	22.16 ± 0.20	−92.5 ± 7.6	−0.56 ± 0.32	−0.61 ± 0.27	5.2	—	− − −	N
246.76058	13.02012	20.32 ± 0.03	19.66 ± 0.03	21.28 ± 0.11	−24.1 ± 6.6	−0.12 ± 0.58	0.94 ± 0.59	3.8	—	−0.68	N
246.09885	12.4867	20.36 ± 0.03	19.66 ± 0.02	21.30 ± 0.10	−98.6 ± 10.7	−1.39 ± 0.47	−1.76 ± 0.44	3.9	—	−0.97	N
247.63172	12.77975	20.40 ± 0.03	19.61 ± 0.02	20.92 ± 0.09	24.5 ± 6.5	0.03 ± 0.34	−0.66 ± 0.29	4.8	—	−3.75	Y
246.37557	13.19678	19.49 ± 0.02	18.39 ± 0.01	20.89 ± 0.06	−67.7 ± 5.8	0.54 ± 0.21	−0.28 ± 0.18	10.0	—	−0.94	N
246.84517	13.6051	20.46 ± 0.03	19.84 ± 0.03	21.27 ± 0.09	−17.0 ± 13.0	−0.86 ± 0.47	−1.76 ± 0.40	3.3	—	−1.12	N
246.75478	12.66005	20.12 ± 0.02	18.98 ± 0.02	21.82 ± 0.16	60.1 ± 4.3	−1.58 ± 0.32	−0.07 ± 0.32	13.5	—	−0.43	N
246.73328	12.5240	20.47 ± 0.03	19.43 ± 0.02	21.64 ± 0.16	32.8 ± 10.1	−3.40 ± 0.39	−1.66 ± 0.34	4.0	—	−1.57	N
247.94199	12.17424	19.91 ± 0.02	19.04 ± 0.02	21.10 ± 0.09	−179.5 ± 13.7	−1.80 ± 0.26	−8.55 ± 0.22	5.5	—	−0.76	N
247.25868	12.37304	18.76 ± 0.01	17.58 ± 0.01	20.11 ± 0.05	−41.9 ± 2.9	−5.34 ± 0.19	1.98 ± 0.17	30.7	—	−1.50	N
247.3685	12.30693	20.59 ± 0.03	19.83 ± 0.03	21.87 ± 0.18	19.5 ± 11.3	−2.23 ± 0.58	−1.87 ± 0.51	3.6	—	− − −	N
247.09069	12.44679	20.14 ± 0.02	19.19 ± 0.02	21.38 ± 0.13	−89.2 ± 5.1	−2.02 ± 0.34	−1.79 ± 0.35	8.7	—	−0.96	N
246.96076	12.66072	18.98 ± 0.01	17.63 ± 0.01	19.92 ± 0.04	−119.4 ± 5.4	−3.33 ± 0.16	−6.12 ± 0.16	11.7	—	− − −	N
248.14307	11.9990	19.69 ± 0.02	18.56 ± 0.01	21.39 ± 0.12	8.3 ± 7.7	0.25 ± 0.19	−4.60 ± 0.16	7.2	—	−0.38	N
246.9166	12.27304	20.63 ± 0.03	19.97 ± 0.03	21.56 ± 0.12	162.4 ± 8.4	−9.39 ± 0.62	2.74 ± 0.62	4.2	—	−0.79	N
246.94378	12.82228	18.64 ± 0.01	17.38 ± 0.01	20.30 ± 0.05	−4.6 ± 2.8	−4.79 ± 0.12	−0.57 ± 0.10	35.9	—	−0.92	N
246.89183	12.85064	20.11 ± 0.02	19.03 ± 0.02	21.67 ± 0.14	−14.4 ± 6.9	−10.06 ± 0.34	−7.80 ± 0.34	7.1	—	−0.47	N
247.78112	12.04271	19.07 ± 0.01	18.18 ± 0.01	20.34 ± 0.05	−43.4 ± 4.8	−0.57 ± 0.15	−0.63 ± 0.12	11.1	—	−0.53	N
247.54116	12.91777	19.61 ± 0.02	18.48 ± 0.01	20.40 ± 0.05	43.6 ± 3.5	−0.40 ± 0.18	−0.43 ± 0.15	12.8	−3.0 ± 0.5	−3.77	Y
246.6543	12.93348	20.01 ± 0.02	18.84 ± 0.02	21.79 ± 0.18	−61.3 ± 12.2	−2.84 ± 0.28	2.08 ± 0.28	5.7	—	−0.43	N
246.96346	12.70229	18.67 ± 0.01	17.39 ± 0.01	20.41 ± 0.06	−9.7 ± 3.3	14.1 ± 0.11	−9.86 ± 0.11	35.5	—	−0.80	N
246.87751	12.65129	20.15 ± 0.02	19.57 ± 0.02	20.93 ± 0.08	−32.1 ± 10.2	−3.91 ± 0.39	−7.20 ± 0.37	10.2	—	−1.03	N
246.86191	12.59161	21.46 ± 0.08	20.48 ± 0.05	22.04 ± 0.17	6.5 ± 5.7	−3.34 ± 1.08	0.03 ± 1.12	11.0	—	− − −	N
246.72922	12.55599	20.48 ± 0.03	19.74 ± 0.03	21.22 ± 0.11	−27.7 ± 9.8	−7.67 ± 0.51	−15.18 ± 0.43	3.6	—	−2.10	N
246.76616	12.68591	20.14 ± 0.02	19.21 ± 0.02	21.15 ± 0.10	−139.7 ± 11.7	−2.68 ± 0.35	−5.32 ± 0.34	8.4	—	−1.72	N
246.71304	12.56697	18.76 ± 0.01	17.45 ± 0.01	20.47 ± 0.06	47.5 ± 4.6	−3.14 ± 0.49	−3.32 ± 0.45	28.2	—	−0.89	N
246.64344	12.68448	19.69 ± 0.02	18.73 ± 0.02	21.06 ± 0.09	77.9 ± 9.3	−9.38 ± 0.23	−18.51 ± 0.21	7.0	—	−0.53	N
247.26691	12.30981	20.02 ± 0.02	18.98 ± 0.02	21.61 ± 0.16	−1.9 ± 8.6	−0.98 ± 0.28	−8.82 ± 0.26	4.5	—	−0.20	N
248.58387	12.5407	20.20 ± 0.02	19.36 ± 0.02	21.32 ± 0.10	12.4 ± 7.2	−1.63 ± 0.33	3.95 ± 0.26	4.3	—	−0.94	N
248.38652	11.94489	19.46 ± 0.02	18.51 ± 0.02	20.95 ± 0.07	−70.1 ± 13.2	0.17 ± 0.16	−7.85 ± 0.13	6.7	—	−0.12	N
247.18706	13.24547	19.87 ± 0.02	18.99 ± 0.02	20.60 ± 0.06	34.9 ± 9.9	−4.23 ± 0.25	−20.18 ± 0.22	10.4	—	−2.92	N
248.95752	11.67386	19.11 ± 0.01	18.23 ± 0.01	20.33 ± 0.04	−92.6 ± 8.7	−0.27 ± 0.13	−0.04 ± 0.10	6.6	—	−0.79	N
246.86297	12.24227	19.59 ± 0.02	18.64 ± 0.02	20.83 ± 0.07	2.3 ± 7.7	−0.40 ± 0.25	−0.84 ± 0.22	5.5	—	−1.00	N
247.09492	13.14445	19.20 ± 0.01	17.93 ± 0.01	20.64 ± 0.07	−115.9 ± 5.1	−10.09 ± 0.12	−1.63 ± 0.10	13.2	—	−1.49	N
247.05246	13.13164	19.69 ± 0.02	18.65 ± 0.01	21.23 ± 0.11	−21.2 ± 14.6	0.38 ± 0.18	−6.83 ± 0.16	4.9	—	−0.34	N
246.98739	13.1295	20.21 ± 0.02	19.13 ± 0.02	21.76 ± 0.18	−75.7 ± 7.2	−2.83 ± 0.27	−2.65 ± 0.25	7.7	—	−0.48	N

Table 3 – *continued*

RA (deg)	DEC (deg)	$g_0^{\rm SDSS}$	$i_0^{\rm SDSS}$	CaHK$_0$	$v_{\rm r}$ (km s^{-1})	μ_α^* (mas yr^{-1})	μ_δ (mas yr^{-1})	S/N	[Fe/H]$_{1+2}^{\rm spectro}$	[Fe/H]$_{\rm Pristine}$	Member
247.01672	13.19916	20.57 ± 0.03	19.81 ± 0.03	21.22 ± 0.11	−2.2 ± 9.0	−2.99 ± 0.42	−5.14 ± 0.35	4.2	—	−2.61	N
248.58885	11.90728	20.16 ± 0.02	19.38 ± 0.02	20.97 ± 0.09	−116.9 ± 13.1	−6.75 ± 0.32	1.23 ± 0.24	4.1	—	−1.95	N
246.73081	13.19528	20.27 ± 0.02	19.31 ± 0.02	21.25 ± 0.09	−32.8 ± 9.2	−0.48 ± 0.52	−8.25 ± 0.47	5.3	—	−1.99	N
248.48765	11.8842	20.15 ± 0.03	19.16 ± 0.02	21.39 ± 0.12	21.3 ± 9.2	5.37 ± 0.28	−7.26 ± 0.22	4.5	—	−1.14	N
246.68288	12.88727	18.99 ± 0.01	17.72 ± 0.01	20.69 ± 0.06	−18.3 ± 2.8	−13.58 ± 0.20	−8.94 ± 0.20	21.5	—	−0.87	N
246.88408	12.59174	20.30 ± 0.03	19.38 ± 0.02	21.50 ± 0.12	−30.6 ± 6.7	−4.46 ± 0.40	−5.21 ± 0.38	7.2	—	−1.04	N
246.88673	12.70166	20.40 ± 0.03	19.55 ± 0.02	21.86 ± 0.16	−94.7 ± 9.4	−9.56 ± 0.47	−1.39 ± 0.42	4.1	—	−− −	N
246.86038	12.65564	20.69 ± 0.03	19.81 ± 0.02	21.93 ± 0.16	−98.8 ± 6.7	−17.02 ± 0.52	−3.90 ± 0.50	6.0	—	−0.68	N
246.82742	12.60486	19.89 ± 0.02	18.91 ± 0.02	21.04 ± 0.09	57.4 ± 7.5	−2.10 ± 0.29	−4.44 ± 0.30	6.9	—	−1.33	N
248.5845	12.59069	20.00 ± 0.02	19.26 ± 0.02	22.51 ± 0.24	74.7 ± 14.0	−2.35 ± 0.28	−6.53 ± 0.22	4.0	—	−− −	N
248.55005	12.5758	19.43 ± 0.02	18.27 ± 0.01	21.06 ± 0.08	−86.1 ± 5.5	3.30 ± 0.17	−6.11 ± 0.13	11.1	—	−0.66	N
247.09157	12.30991	19.13 ± 0.01	18.09 ± 0.01	20.49 ± 0.06	−1.4 ± 3.1	−4.88 ± 0.28	3.45 ± 0.29	20.9	—	−0.97	N
248.35298	12.51463	19.51 ± 0.02	18.18 ± 0.01	20.61 ± 0.06	−37.8 ± 5.9	−8.14 ± 0.12	−0.23 ± 0.10	12.6	—	−3.45	N
247.03553	12.31056	20.77 ± 0.03	19.93 ± 0.03	21.54 ± 0.13	−101.7 ± 7.8	−4.51 ± 0.62	−5.41 ± 0.63	3.5	—	−2.46	N
246.74741	12.44978	20.98 ± 0.04	20.29 ± 0.04	21.58 ± 0.15	−37.6 ± 8.3	0.60 ± 0.66	−1.06 ± 0.54	5.7	—	−2.53	?
246.74694	12.31479	20.49 ± 0.03	19.46 ± 0.02	21.71 ± 0.16	−116.6 ± 10.4	−2.73 ± 0.42	−13.1 ± 0.36	4.8	—	−1.40	N
246.69844	12.43831	19.18 ± 0.01	18.06 ± 0.01	20.66 ± 0.07	44.9 ± 3.5	−1.07 ± 0.15	−9.50 ± 0.13	14.3	—	−0.83	N
248.46686	12.0008	19.52 ± 0.02	18.55 ± 0.01	21.04 ± 0.08	27.7 ± 4.7	1.95 ± 0.18	−0.05 ± 0.14	6.8	—	−0.13	N
247.19971	13.52296	19.47 ± 0.02	18.56 ± 0.01	20.79 ± 0.07	−103.1 ± 8.7	−5.88 ± 0.18	−2.08 ± 0.14	7.7	—	−0.45	N
247.19206	13.44977	19.90 ± 0.02	18.75 ± 0.02	21.43 ± 0.11	−55.4 ± 6.6	−5.25 ± 0.20	−12.62 ± 0.17	8.9	—	−0.78	N
247.24622	13.41695	19.93 ± 0.02	18.69 ± 0.02	21.69 ± 0.14	−81.0 ± 6.5	−0.28 ± 0.20	−7.97 ± 0.17	8.1	—	−0.63	N
247.21778	13.57619	20.49 ± 0.03	19.66 ± 0.02	21.57 ± 0.14	−141.8 ± 6.8	−10.34 ± 0.40	−12.98 ± 0.33	4.6	—	−1.02	N
247.88895	12.21281	19.37 ± 0.02	18.08 ± 0.01	21.01 ± 0.08	31.2 ± 5.1	−5.15 ± 0.15	−3.20 ± 0.12	14.0	—	−1.04	N
247.83506	12.03185	20.20 ± 0.02	19.35 ± 0.02	21.40 ± 0.11	12.7 ± 11.8	−0.69 ± 0.35	−1.91 ± 0.27	4.1	—	−0.66	N
247.4585	13.70662	19.67 ± 0.02	18.62 ± 0.02	20.54 ± 0.06	48.8 ± 6.1	−0.20 ± 0.20	−0.40 ± 0.17	8.7	—	−3.03	Y
248.58076	13.1713	19.03 ± 0.01	17.99 ± 0.01	20.57 ± 0.06	−45.7 ± 9.9	−9.11 ± 0.12	−0.52 ± 0.10	7.3	—	−0.32	N
247.28533	13.26492	20.29 ± 0.03	19.11 ± 0.02	20.93 ± 0.08	−132.1 ± 7.6	−8.18 ± 0.21	−13.54 ± 0.18	8.8	—	−− −	N
247.24962	13.33747	19.97 ± 0.02	19.08 ± 0.02	21.25 ± 0.10	−100.0 ± 7.7	−3.55 ± 0.24	−3.44 ± 0.21	4.3	—	−0.52	N
246.85571	13.3048	20.50 ± 0.03	19.40 ± 0.02	21.93 ± 0.16	14.3 ± 6.1	−0.82 ± 0.38	−6.16 ± 0.35	5.3	—	−0.90	N
246.68136	13.33053	19.96 ± 0.02	18.78 ± 0.02	21.67 ± 0.15	0.2 ± 11.9	−5.99 ± 0.26	−0.21 ± 0.27	4.2	—	−0.54	N
248.57357	13.39772	18.58 ± 0.01	17.19 ± 0.01	20.41 ± 0.06	−31.1 ± 4.2	−2.59 ± 0.08	−18.44 ± 0.07	13.2	—	−0.90	N
246.95402	12.63921	18.45 ± 0.01	17.12 ± 0.01	20.82 ± 0.08	3.7 ± 5.0	−10.3 ± 0.09	−9.15 ± 0.09	35.7	—	−− −	N
247.55111	13.20879	20.64 ± 0.03	19.97 ± 0.03	21.46 ± 0.11	−90.1 ± 8.2	−1.42 ± 0.42	−1.42 ± 0.35	3.1	—	−1.40	N
246.87513	12.71872	18.76 ± 0.01	17.29 ± 0.01	20.57 ± 0.06	−45.9 ± 4.0	−6.27 ± 0.11	6.73 ± 0.11	28.3	—	−1.09	N
246.8359	12.71057	19.94 ± 0.02	18.70 ± 0.02	21.22 ± 0.10	−45.9 ± 5.2	−3.98 ± 0.24	0.93 ± 0.23	9.2	—	−1.95	N
246.79782	12.75613	19.71 ± 0.02	18.40 ± 0.01	21.24 ± 0.10	−51.8 ± 4.5	−1.81 ± 0.22	−8.74 ± 0.21	11.4	—	−1.42	N
246.68838	12.63302	20.01 ± 0.03	19.11 ± 0.02	21.10 ± 0.09	−185.5 ± 7.8	−7.45 ± 0.33	−19.2 ± 0.29	10.0	—	−1.34	N
247.25876	13.61103	20.14 ± 0.02	19.38 ± 0.02	21.23 ± 0.10	−119.6 ± 7.3	−5.68 ± 0.30	−3.78 ± 0.25	5.4	—	−0.71	N
248.58281	12.69705	19.54 ± 0.02	18.31 ± 0.01	21.35 ± 0.12	−10.0 ± 6.6	7.08 ± 0.15	−9.65 ± 0.13	10.7	—	−0.57	N
246.08627	12.41528	19.78 ± 0.02	18.44 ± 0.01	21.36 ± 0.10	−142.5 ± 5.4	0.24 ± 0.23	0.40 ± 0.22	10.4	—	−1.38	?
246.89308	13.50018	20.32 ± 0.02	19.24 ± 0.02	21.57 ± 0.12	31.6 ± 9.0	−6.40 ± 0.28	−12.21 ± 0.25	5.4	—	−1.45	N

Table 3 – *continued*

RA (deg)	DEC (deg)	$g_0^{\rm SDSS}$	$i_0^{\rm SDSS}$	CaHK$_0$	$v_{\rm r}$ (km s^{-1})	μ_α^* (mas yr^{-1})	μ_δ (mas yr^{-1})	S/N	[Fe/H]$_{1+2}^{\rm spectro}$	[Fe/H]$_{\rm Pristine}$	Member
246.74212	13.48835	18.80 ± 0.01	17.40 ± 0.01	20.52 ± 0.07	−19.1 ± 3.0	−3.22 ± 0.09	−2.08 ± 0.08	18.8	—	−1.15	N
247.47233	13.79749	20.47 ± 0.03	19.39 ± 0.02	21.84 ± 0.18	−60.9 ± 13.0	−4.74 ± 0.34	0.99 ± 0.30	3.4	—	−1.00	N
247.15456	13.78807	19.71 ± 0.02	18.97 ± 0.02	20.93 ± 0.09	−127.6 ± 11.7	−2.51 ± 0.25	−2.06 ± 0.22	4.7	—	−0.23	N
247.12676	13.77042	19.90 ± 0.02	18.83 ± 0.02	21.53 ± 0.15	7.8 ± 6.1	−1.34 ± 0.24	−6.68 ± 0.19	8.2	—	−0.25	N
246.96895	13.72795	20.60 ± 0.03	19.48 ± 0.02	21.80 ± 0.16	−154.3 ± 7.0	−0.76 ± 0.37	−23.09 ± 0.31	4.7	—	−1.92	N
246.91982	13.86001	19.80 ± 0.02	18.99 ± 0.02	20.78 ± 0.07	−105.8 ± 7.3	−8.66 ± 0.24	4.08 ± 0.22	5.5	—	−1.40	N
248.59121	12.96194	19.99 ± 0.02	18.78 ± 0.02	21.72 ± 0.16	−4.2 ± 10.1	2.75 ± 0.21	−11.55 ± 0.18	5.5	—	−0.59	N
246.77069	13.90807	19.27 ± 0.02	17.95 ± 0.01	20.66 ± 0.07	80.8 ± 4.2	−3.15 ± 0.15	−6.56 ± 0.13	20.0	—	−1.62	N
246.75267	13.85352	19.94 ± 0.02	18.72 ± 0.02	21.52 ± 0.14	−28.6 ± 9.9	−3.53 ± 0.22	−4.82 ± 0.18	6.4	—	−0.87	N
246.62949	13.82289	19.36 ± 0.02	18.15 ± 0.01	21.03 ± 0.09	−30.8 ± 3.6	0.58 ± 0.14	−5.84 ± 0.12	15.9	—	−0.74	N
246.69948	13.80275	20.53 ± 0.03	19.84 ± 0.03	21.13 ± 0.10	−86.0 ± 14.6	−1.38 ± 0.48	−1.08 ± 0.43	4.0	—	−2.52	N
246.66877	13.37787	20.08 ± 0.02	18.86 ± 0.02	21.49 ± 0.13	−106.3 ± 9.0	−3.64 ± 0.28	−6.16 ± 0.29	7.0	—	−1.43	N
248.71753	12.63136	19.71 ± 0.02	18.67 ± 0.02	21.13 ± 0.12	6.1 ± 8.0	−1.18 ± 0.19	−10.98 ± 0.16	6.3	—	−0.81	N
248.7167	12.4921	20.11 ± 0.02	19.20 ± 0.02	21.48 ± 0.14	37.7 ± 7.0	−4.54 ± 0.31	−0.15 ± 0.24	6.8	—	−0.28	N
248.70384	12.49582	20.58 ± 0.03	19.75 ± 0.02	21.82 ± 0.18	−59.2 ± 11.3	0.16 ± 0.44	−11.94 ± 0.35	4.2	—	−0.48	N
246.66737	13.47796	19.06 ± 0.01	17.86 ± 0.01	20.57 ± 0.06	33.8 ± 3.2	−0.50 ± 0.12	−0.40 ± 0.11	14.8	—	−0.91	N
248.91509	12.19686	18.80 ± 0.01	17.46 ± 0.01	20.49 ± 0.05	−13.5 ± 4.1	−5.15 ± 0.09	−2.03 ± 0.07	16.5	—	−1.09	N
248.84188	12.35783	19.05 ± 0.01	17.69 ± 0.01	20.79 ± 0.07	−103.4 ± 4.1	−5.67 ± 0.64	−2.20 ± 0.53	28.4	—	−1.03	N
248.91006	12.27981	20.33 ± 0.03	19.36 ± 0.02	21.65 ± 0.13	−173.7 ± 9.9	−5.92 ± 0.33	−10.56 ± 0.28	7.7	—	−0.81	N
248.84028	12.30854	20.75 ± 0.03	19.80 ± 0.03	21.86 ± 0.17	−2.2 ± 6.9	−0.13 ± 0.43	−18.92 ± 0.34	3.6	—	−1.43	N
248.72804	12.25439	20.10 ± 0.03	19.08 ± 0.02	21.44 ± 0.10	6.9 ± 7.9	−4.84 ± 0.26	−6.29 ± 0.20	8.1	—	−0.97	N
248.52523	12.32225	19.78 ± 0.02	18.89 ± 0.02	21.16 ± 0.09	−17.2 ± 8.6	0.01 ± 0.23	−7.70 ± 0.18	4.7	—	−0.24	N
247.0681	12.58077	20.05 ± 0.02	19.10 ± 0.02	21.52 ± 0.15	−6.5 ± 5.8	−0.38 ± 0.36	−0.51 ± 0.35	8.9	—	−0.21	N
246.9519	12.54664	20.62 ± 0.03	19.94 ± 0.03	21.69 ± 0.16	21.6 ± 11.3	1.19 ± 0.68	−16.94 ± 0.61	5.7	—	−0.23	N
248.73247	12.63949	19.76 ± 0.02	18.80 ± 0.02	21.40 ± 0.15	−58.8 ± 7.6	0.14 ± 0.20	−0.54 ± 0.16	5.9	—	−− −	N
246.50552	13.50975	19.81 ± 0.02	19.03 ± 0.02	20.78 ± 0.05	6.3 ± 8.7	−1.08 ± 0.29	−1.04 ± 0.31	6.7	—	−1.28	N
248.84095	11.93982	19.71 ± 0.02	18.65 ± 0.01	21.00 ± 0.08	0.7 ± 6.4	−0.60 ± 0.19	−1.84 ± 0.15	9.2	—	−1.23	N
248.73755	12.10452	18.86 ± 0.01	17.88 ± 0.01	20.27 ± 0.05	9.1 ± 3.4	−2.00 ± 0.10	−14.28 ± 0.08	18.2	—	−0.52	N
248.7234	12.07086	20.90 ± 0.05	20.42 ± 0.05	22.22 ± 0.24	−154.9 ± 11.4	−4.37 ± 0.52	−5.11 ± 0.45	3.2	—	−− −	N
248.75347	12.09482	20.20 ± 0.02	19.15 ± 0.02	21.45 ± 0.11	−27.2 ± 9.2	−1.99 ± 0.28	−7.75 ± 0.22	9.3	—	−1.37	N
247.08649	12.6308	20.09 ± 0.02	19.08 ± 0.02	21.39 ± 0.12	45.5 ± 7.0	1.66 ± 0.33	−4.65 ± 0.31	7.1	—	−1.08	N
248.78168	11.71213	20.03 ± 0.02	18.83 ± 0.02	21.43 ± 0.11	−18.9 ± 12.0	3.46 ± 0.19	−7.15 ± 0.16	5.5	—	−1.40	N
247.01658	12.58344	19.91 ± 0.02	18.94 ± 0.02	21.26 ± 0.11	14.3 ± 5.9	−4.39 ± 0.29	−4.00 ± 0.28	5.4	—	−0.71	N
246.99728	12.74368	20.24 ± 0.02	19.43 ± 0.02	21.61 ± 0.15	−110.9 ± 4.1	−2.32 ± 0.44	−9.32 ± 0.38	7.0	—	−− −	N
247.03631	12.0440	19.87 ± 0.02	18.66 ± 0.02	21.44 ± 0.12	−46.5 ± 5.5	−4.04 ± 0.25	−1.22 ± 0.24	10.8	—	−0.88	N
248.84067	11.87536	19.72 ± 0.02	18.87 ± 0.02	20.67 ± 0.06	−145.0 ± 12.3	−17.14 ± 0.20	−15.86 ± 0.16	5.9	—	−1.63	N
248.9065	12.9504	20.04 ± 0.02	19.01 ± 0.02	21.66 ± 0.13	39.4 ± 9.4	−0.69 ± 0.26	−1.39 ± 0.23	4.1	—	−0.12	N
247.13655	12.73514	19.51 ± 0.02	18.62 ± 0.01	20.89 ± 0.09	−0.3 ± 5.7	−6.45 ± 0.22	−0.28 ± 0.21	11.3	—	−0.23	N
248.90786	12.54507	20.05 ± 0.03	19.22 ± 0.02	20.83 ± 0.07	72.8 ± 11.2	0.84 ± 0.29	−4.89 ± 0.24	5.0	—	−2.30	N

Table 3 – *continued*

RA (deg)	DEC (deg)	$g_0^{\rm SDSS}$	$i_0^{\rm SDSS}$	CaHK$_0$	$v_{\rm r}$ (km s^{-1})	μ_α^* (mas yr^{-1})	μ_δ (mas yr^{-1})	S/N	[Fe/H]$_{1+2}^{\rm spectro}$	[Fe/H]$_{\rm Pristine}$	Member
248.85394	12.71637	20.75 ± 0.03	19.79 ± 0.03	21.46 ± 0.11	−24.6 ± 7.1	−9.28 ± 0.51	4.14 ± 0.45	4.9	—	−3.70	N
248.77785	12.59378	20.53 ± 0.03	19.75 ± 0.03	21.24 ± 0.10	−14.7 ± 11.7	−1.89 ± 0.39	−1.16 ± 0.32	3.1	—	−2.48	N
248.77866	12.69494	20.10 ± 0.02	19.18 ± 0.02	21.51 ± 0.16	−19.5 ± 14.0	−0.81 ± 0.27	−10.37 ± 0.22	6.6	—	−0.22	N
248.76673	12.70066	20.23 ± 0.02	19.15 ± 0.02	21.48 ± 0.11	−80.4 ± 7.1	−6.90 ± 0.27	−12.16 ± 0.22	7.7	—	−1.47	N
248.67474	12.59263	20.35 ± 0.03	19.26 ± 0.02	21.89 ± 0.15	−13.3 ± 6.3	−1.96 ± 0.30	−10.58 ± 0.24	3.5	—	−0.64	N
246.34015	12.9162	19.91 ± 0.02	19.11 ± 0.02	20.95 ± 0.07	−22.0 ± 6.7	0.15 ± 0.29	−0.37 ± 0.26	5.2	—	−1.05	N
248.86753	12.37052	20.12 ± 0.02	19.13 ± 0.02	21.40 ± 0.11	−96.8 ± 5.5	0.19 ± 0.26	−1.53 ± 0.21	6.5	—	−1.04	N
248.8243	12.33862	20.03 ± 0.02	18.84 ± 0.02	21.60 ± 0.13	−25.8 ± 5.7	−1.17 ± 0.22	−4.78 ± 0.18	7.3	—	−0.80	N
248.50171	12.41356	19.29 ± 0.02	18.35 ± 0.01	20.60 ± 0.06	7.1 ± 12.5	−1.74 ± 0.33	−7.39 ± 0.27	6.7	—	−0.65	N
248.88532	12.01262	19.14 ± 0.02	17.68 ± 0.01	20.88 ± 0.07	4.6 ± 3.0	−3.92 ± 0.11	−7.39 ± 0.08	18.7	—	−1.20	N
248.8507	11.99434	19.57 ± 0.02	18.58 ± 0.02	20.94 ± 0.07	−118.8 ± 8.7	−11.57 ± 0.16	−7.94 ± 0.13	9.6	—	−0.69	N
248.90659	12.19325	19.74 ± 0.02	18.58 ± 0.02	21.07 ± 0.08	13.8 ± 5.4	7.14 ± 0.16	−17.43 ± 0.14	10.4	—	−1.53	N
248.62262	12.20119	19.91 ± 0.02	19.06 ± 0.02	21.11 ± 0.08	−4.3 ± 8.6	−1.32 ± 0.23	−11.64 ± 0.18	3.9	—	−0.65	N
248.66906	12.1607	20.26 ± 0.02	19.33 ± 0.02	21.51 ± 0.12	−96.2 ± 13.4	−8.47 ± 0.28	−6.32 ± 0.23	5.3	—	−0.83	N
246.94712	12.75213	20.05 ± 0.02	18.88 ± 0.02	21.42 ± 0.13	14.7 ± 3.4	−8.32 ± 0.29	−2.07 ± 0.29	13.5	—	−1.38	N
248.84995	13.20057	18.59 ± 0.01	17.30 ± 0.01	19.85 ± 0.04	−4.0 ± 10.7	−13.26 ± 0.08	8.80 ± 0.07	11.2	—	−2.14	N
248.90558	13.05926	19.63 ± 0.02	17.49 ± 0.01	20.74 ± 0.09	42.7 ± 4.6	−6.81 ± 0.10	−7.38 ± 0.08	20.6	—	− − −	N
247.03244	13.73306	20.43 ± 0.03	19.57 ± 0.03	21.25 ± 0.12	−113.3 ± 9.3	−1.78 ± 0.36	−26.46 ± 0.30	4.5	—	−2.32	N
248.55112	13.0871	19.25 ± 0.02	18.03 ± 0.01	20.97 ± 0.10	−150.2 ± 10.7	2.77 ± 0.13	−7.28 ± 0.11	10.6	—	−0.66	N
247.2214	13.65181	20.22 ± 0.03	19.32 ± 0.02	21.33 ± 0.11	−172.9 ± 10.7	−5.87 ± 0.29	−12.11 ± 0.24	7.1	—	−1.26	N
247.1671	13.54161	19.88 ± 0.02	18.60 ± 0.01	21.44 ± 0.12	−79.6 ± 4.4	−6.13 ± 0.19	7.27 ± 0.16	9.7	—	−1.22	N
247.08076	13.56689	19.85 ± 0.02	18.92 ± 0.02	21.05 ± 0.11	−175.3 ± 8.1	−5.30 ± 0.23	−5.02 ± 0.19	8.8	—	−0.99	N
248.9193	12.76459	19.79 ± 0.02	18.84 ± 0.02	20.97 ± 0.08	−19.4 ± 8.2	−1.43 ± 0.23	−3.29 ± 0.18	7.5	—	−1.20	N
248.93277	12.00676	20.11 ± 0.02	19.40 ± 0.02	20.97 ± 0.06	−244.9 ± 12.2	−0.90 ± 0.30	−0.85 ± 0.22	3.6	—	−1.40	N
247.17602	13.02714	19.72 ± 0.02	18.61 ± 0.01	21.05 ± 0.09	−3.8 ± 6.5	−2.49 ± 0.18	−5.43 ± 0.16	12.5	—	−1.27	N
247.6062	12.33472	19.51 ± 0.02	18.45 ± 0.02	20.27 ± 0.05	235.1 ± 13.0	0.43 ± 0.61	−0.49 ± 0.51	9.0	—	−3.71	N
247.03182	13.01717	18.47 ± 0.01	17.14 ± 0.01	20.09 ± 0.05	−26.2 ± 11.1	−3.20 ± 0.15	−1.52 ± 0.13	38.8	—	−1.21	N
247.52398	12.2559	20.70 ± 0.03	19.95 ± 0.03	21.23 ± 0.10	−57.0 ± 5.1	−4.88 ± 0.57	−9.70 ± 0.48	6.5	—	−3.37	N
248.86556	12.85928	19.77 ± 0.02	18.46 ± 0.01	21.32 ± 0.10	−55.4 ± 7.8	−2.74 ± 0.15	−4.24 ± 0.13	11.2	—	−1.35	N
248.85031	12.50588	20.07 ± 0.03	19.16 ± 0.02	21.23 ± 0.10	−0.6 ± 6.9	−6.46 ± 0.29	−4.05 ± 0.23	6.1	—	−1.09	N
248.80693	12.50851	20.38 ± 0.03	19.42 ± 0.03	21.66 ± 0.16	−185.5 ± 7.6	−3.00 ± 0.46	−8.04 ± 0.39	5.8	—	−0.92	N
248.63792	12.49248	19.98 ± 0.02	18.79 ± 0.02	21.53 ± 0.13	28.5 ± 11.1	−8.27 ± 0.22	−7.02 ± 0.18	6.0	—	−0.84	N
248.37505	12.37005	20.03 ± 0.02	18.82 ± 0.02	21.54 ± 0.12	15.2 ± 5.9	−1.65 ± 0.22	−2.46 ± 0.17	4.2	—	−1.01	N
248.39447	13.15989	20.02 ± 0.03	18.85 ± 0.02	21.47 ± 0.12	20.3 ± 12.7	7.06 ± 0.20	−14.83 ± 0.16	4.0	—	−1.04	N

Table 4. Probable misidentified member stars from the literature. The mention 'CaHK' in the last column indicates that the CaHK is decisive in the decision-making, 'PM' that the proper motion is.

RA (deg)	DEC (deg)	$g_0^{\rm SDSS}$	$i_0^{\rm SDSS}$	$\rm CaHK_0$	$v_{\rm r}$ (km s^{-1})	μ_α^* (mas yr^{-1})	μ_δ (mas yr^{-1})	$\rm [Fe/H]_{spectro}$	
247.79628	12.78814	19.39 ± 0.02	18.15 ± 0.01	21.17 ± 0.10	30.7 ± 2.2	-17.57 ± 0.14	-17.67 ± 0.12	-1.5 ± 0.2	PM
247.9701	12.7466	21.12 ± 0.04	21.56 ± 0.10	21.29 ± 0.13	7.0 ± 11.0	—	—	—	CaHK
247.7754	12.7951	21.09 ± 0.04	21.53 ± 0.12	21.56 ± 0.17	61.0 ± 13.0	—	—	—	CaHK
247.7699	12.7390	21.12 ± 0.04	21.50 ± 0.11	21.23 ± 0.12	40.0 ± 14.0	—	—	—	CaHK
247.7605	12.8298	21.16 ± 0.04	21.53 ± 0.09	21.40 ± 0.13	31.0 ± 12.0	—	—	—	CaHK
247.7493	12.7674	20.21 ± 0.02	20.26 ± 0.03	20.10 ± 0.04	64.0 ± 8.0	0.01 ± 0.62	-0.60 ± 0.51	—	CaHK
247.7242	12.8450	20.64 ± 0.03	20.25 ± 0.03	20.91 ± 0.10	65.0 ± 10.0	-0.50 ± 0.68	-0.11 ± 0.56	—	CaHK
247.5792	12.8839	21.08 ± 0.04	21.04 ± 0.08	21.40 ± 0.11	80.0 ± 12.0	—	—	—	CaHK
247.7566	12.7861	21.94 ± 0.08	21.37 ± 0.08	22.50 ± 0.05	41.4 ± 3.1	—	—	—	CaHK
247.7758	12.8086	22.25 ± 0.10	21.40 ± 0.10	23.42 ± 0.10	48.5 ± 3.5	—	—	—	CaHK
247.6033	12.8864	20.83 ± 0.03	19.89 ± 0.03	22.03 ± 0.19	53.1 ± 2.5	3.82 ± 0.61	-20.14 ± 0.50	-1.3 ± 0.1	PM
247.7911	12.7951	20.80 ± 0.03	20.04 ± 0.03	21.55 ± 0.15	41.0 ± 6.2	-0.37 ± 0.50	-0.44 ± 0.44	—	CaHK

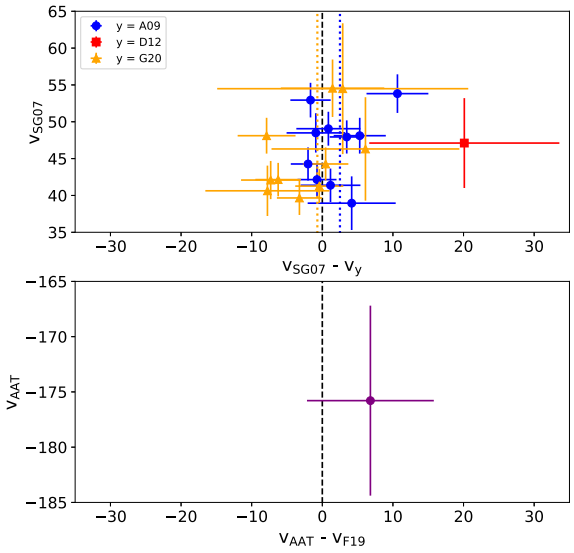

Figure 9. Upper panel: heliocentric velocity differences between the sample of Simon & Geha (2007) and the ones of Adén et al. 2009a (A09, blue circles), Deason et al. 2012 (D12, red squares), and Gregory et al. 2020 (G20, orange triangles). Lower panel: heliocentric velocity difference of a star in common between the new AAT sample and the one of Fu et al. (2019). The central dashed black line shows the identity. Coloured dotted lines show the final offset found for each sample. Differences larger than 20 km s^{-1} have been excluded as they most likely reflect poor fitting on one or both side(s).

described in equations (2) and (3):

$$\mathcal{L}(\mathrm{v}_{\mathrm{r},k}, \delta_{\mathrm{v},k} | \langle \mathrm{v}_{\mathrm{Her}} \rangle, \langle \mathrm{v}_{\mathrm{MW}} \rangle, \sigma_{\mathrm{v}}^{\mathrm{Her}}, \sigma_{\mathrm{v}}^{\mathrm{MW}}, \mathrm{d}v/\mathrm{d}\chi, \theta, \eta_{\mathrm{Her}})$$
$$= \prod_k \left[\eta_{\mathrm{Her}} \left(\frac{1}{\sqrt{2\pi\sigma}} \right) \times \exp\left(\frac{1}{2} \Delta_{\mathrm{v}} / \sigma^2 \right) \mathcal{L}_{\mathrm{PM}}^{\mathrm{Her}} \right.$$
$$\left. + (1 - \eta_{\mathrm{Her}}) \mathcal{G}(\mathrm{v}_{\mathrm{r},k}, \delta_{\mathrm{v},k}, \langle \mathrm{v}_{\mathrm{MW}} \rangle, \sigma_{\mathrm{v}}^{\mathrm{MW}}) \mathcal{L}_{\mathrm{PM}}^{\mathrm{MW}} \right], \quad (3)$$

We define Δ_v such that $\Delta_v = v_{\mathrm{r},k} - y \times \mathrm{d}v/\mathrm{d}\chi + \langle v_{\mathrm{Her}} \rangle$ with $\mathrm{d}v/\mathrm{d}\chi$ the systemic heliocentric velocity gradient, and χ the galactocentric distance along the position angle θ. y is the angular distance computed such that $y_k = X_k \sin\theta + Y_k \cos\theta$ and θ the direction of the velocity gradient. We also define $\sigma = \sqrt{(\sigma_{\mathrm{v}}^{\mathrm{Her}} + \delta_{\mathrm{v}}^2)}$. Finally, η_{Her} is the Hercules member fraction of the spectroscopic sample. The velocity gradient defined in such a model corresponds to a linear, monotonic velocity change along the dwarf. We adopt the same convention as previous dynamical analyses of Hercules, i.e. that a positive velocity gradient corresponds to an increase of the velocity towards decreasing RA. A 2000 000 iterations MCMC is performed . Aside from the rejection of unphysical values (negative dispersions are forbidden, and η_{Her} cannot be below 0 or above 1), only uniform priors are adopted. Based on this analysis, a kinematic membership probability can be computed for all stars. Combined with their metallicity properties, they lead to the discovery of three new Hercules members, including one at $\sim 9.5 R_{\mathrm{h}}$ ($\sim$2.1 kpc) of the satellite, computed as the elliptical distance to Hercules' centroid according to the structural parameters of Muñoz et al. (2018). The others lie at $\sim 1.6 R_{\mathrm{h}}$ ($\sim$335 pc) and $\sim 0.5 R_{\mathrm{h}}$ ($\sim$97 pc). We also report three 'uncertain candidates', i.e. stars marginally compatible with Hercules' dynamical properties, but with an unconvincing membership status discussed in Section 4. The locations of these six stars are shown in Figs 1, 7, 8, and 10. The PDFs resulting from the MCMC are shown in Fig. 11.

We find a systemic velocity of $\langle \mathrm{v} \rangle = 45.7^{+2.3}_{-3.7}$ km s^{-1}, an intrinsic velocity dispersion of $8.0^{+1.4}_{-2.0}$ km s^{-1}, at odds with measurements from the literature (5.1 ± 0.9 km s^{-1}). Finally, no significant velocity gradient is detected with an inference of $0.1^{+0.4}_{-0.2}$ km s^{-1} arcmin^{-1}, i.e. $1.6^{+10.0}_{-3.8}$ km s^{-1} kpc^{-1} (26.1 km s^{-1} at the 3σ confidence limit). The posterior PDF for the velocity gradient is shown as the dotted blue line in Fig. 11.

4 MEMBERSHIP ASSESSMENT

Fig. 10 shows the distribution of our AAT sample superimposed with literature members. Two different groups can be identified in the new spectroscopy, those being the new members including all criteria detailed in Section 3.2, and the uncertain candidates. The membership of each star will be discussed individually in what follows.

4.1 The new members Her 3, Her 5, and Her 180

Their properties strongly favour them to be bona-fide members of Hercules. First of all, they lie on the RGB of the UFD (Fig. 1). Their PM and heliocentric velocity membership are also extremely high, i.e. more than 90 per cent in all cases. However, as detailed above, these properties are entangled with the MW. The most compelling evidence of their membership lie in the Pristine photometry presented in Fig. 7, where they lie in a very metal-poor region of the diagram.

Ideally, this would be confirmed by a spectroscopic derivation of their metallicities. While the S/N of Her 5 and Her 180 spectra are slightly too low to yield a reliable metallicity estimate, it is possible for Her 3 (S/N $\sim$12.7) using the calibration presented in this work based on the first two CaT lines. Its spectroscopic metallicity of [Fe/H] $= -3.0 \pm 0.5$ places it well within the MDF of Hercules and in the tail of the MW's (Fig. 4).

The only element of caution regarding Her 5 is its spatial location, as Fig. 1 shows that the star is not located along the major axis of the very elongated UFD while still located at a very large distance ($\sim 9.5 r_{\mathrm{h}}$). This fact is however mitigated by the finding of Garling et al. (2018) and one of their new RR lyrae located well beyond Hercules' tidal radius while also being far off its major axis. Her 3 and Her 180 positions are aligned with the major axis of Hercules.

4.2 The uncertain candidates

We also find three uncertain candidates shown as the orange diamonds in Fig. 10. These stars have a proper motion compatible with that of Hercules but lie at the edge of the CaHK selection detailed in Section 3.2.1, where contamination from the MW is still not unlikely.

Based on their CaHK colour–colour diagram locations, which place them at the edge of the members/non-members region defined in Fig. 7, Her 464 and Her 10 should be significantly more metal-rich than our three new members. However, this is absolutely not reflected in their locations in the CMD of Hercules. Only Her 6 has a coherent CMD location since it is redder than the favoured Hercules isochrone. One of these also have a spectroscopic metallicity measurement (which is only valid if it is considered to be at Hercules' distance) placing it at the metal-rich rail of Hercules' MDF. Such a metallicity would be unlikely for distant members since the metal-rich population is supposed to be more centrally concentrated even in UFDs (Chiti et al. 2021, Longeard et al. 2022). Furthermore, while Her 464's PM uncertainties allow for it to be perfectly compatible with the systemic proper motion of Hercules, the other two stars PMs are slightly less convincing.

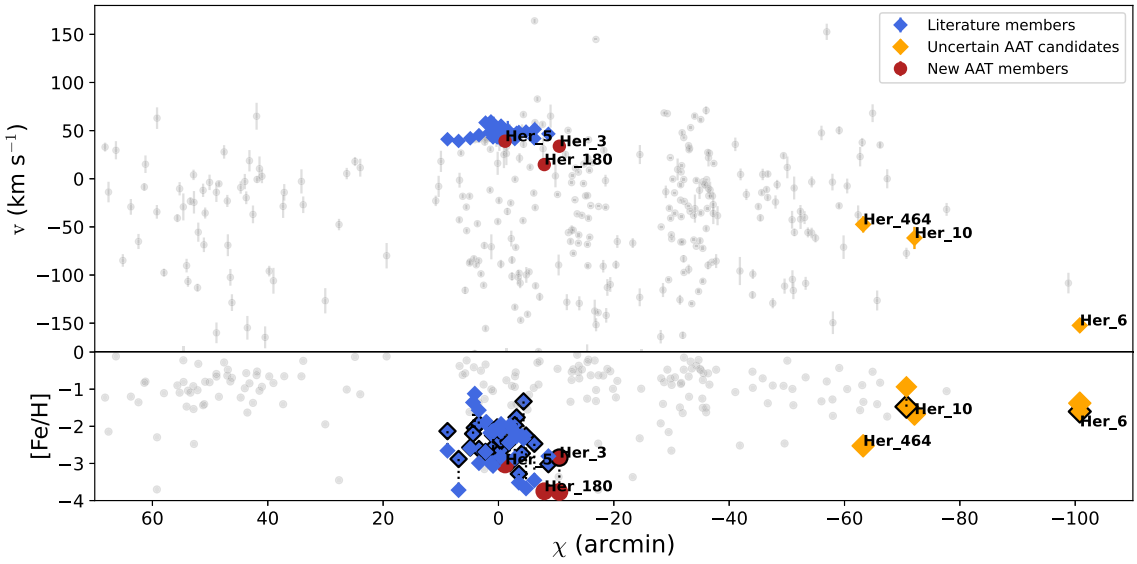

Figure 10. Top panel: phase-space distribution of the AAT + literature non-members (grey), literature members (blue diamonds), AAT uncertain candidates (orange diamonds), and AAT new confirmed members (red circles). χ is defined as a distance respective to a given position angle (see Section 3.2.3). Bottom panel: position versus metallicity. When both photometric and spectroscopic metallicities are available for the same star, they are linked by a vertical dashed black line, with the black-contoured symbols indicating the spectroscopic one.

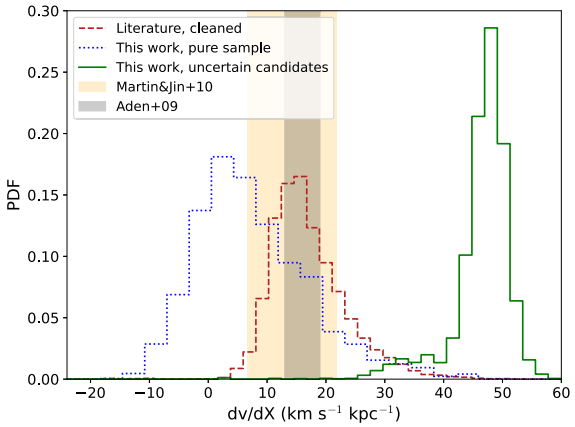

Figure 11. PDFs of the velocity gradient of Hercules in the three cases detailed in Section 5.

Finally, Fig. 10 shows a suspicious spatial gap between −20 and −60 arcmin, i.e. between our confirmed members and the uncertain candidates. The finding of a member in this gap would have brought credit to at least one of the candidates to be members, but even pushing down our kinematic membership probability down to a threshold of 1 per cent (while keeping the CaHK selection) yields no potential members in that area.

For all these reasons, we favour these three stars to not be Hercules members. This decision has an impact of the resulting velocity gradient as shown in the next section.

5 ON THE VELOCITY GRADIENT OF HERCULES

Our measurement is only marginally compatible with the observed gradient of Adén et al. (2009a) (16 ± 3 km s^{-1} kpc^{-1}) at 1.4σ, but does not discard the theoretical ones of Fu et al. (2019) (0.6 km s^{-1} kpc^{-1}) or Küpper et al. (2017) (4.9 km s^{-1} kpc^{-1}). This result is driven by the rejection of 3 stars classified as uncertain candidates. To better understand the impact of this choice, the dynamical modelling analysis detailed in the last section is performed in three different cases:

(i) Only spectroscopy from the literature, cleaned with the *Gaia* selection (when available, Section 3.2.1) but without the CaHK selection (Section 3.2.2) (dashed red line, see Fig. 11)

(ii) The final spectroscopic sample detailed in Section 3.2 including the three uncertain candidates (solid green line).

(iii) The final spectroscopic sample detailed in Section 3.2 without the three uncertain candidates (dotted blue line).

The results are shown in Fig. 11. It confirms that our analysis is consistent with previous studies as using only the literature spectroscopy combined *Gaia* yields a similar gradient as the ones found by Adén et al. (2009a) and Martin & Jin (2010). However, once the AAT data and the metallicity-sensitive, CaHK photometry are introduced, two cases are possible. If the three uncertain stars at large distances are considered as members, then a significant velocity gradient is found ($45.9^{+2.7}_{-2.6}$ km s^{-1} kpc^{-1}). However, if they are considered as MW contaminants, no statistically significant gradient is found. Given the large doubt casted on their membership as detailed in Section 4, this hypothesis is favoured.

6 DISCUSSION AND CONCLUSION

We present in this work new medium resolution spectroscopy of the faint and extremely elongated UFD Hercules with the AAT and its 2dF spectrograph. A total of 175 spectra with SNR ≥3 of high and low-probability potential members were analysed as far as ∼13 r_h of the UFD. This new sample is then combined with all available literature data sets. The CMD location, PM, and metallicity-sensitive, CaHK magnitude of each star are used to clean the spectroscopy from obvious contaminants. While the velocities and PMs of Hercules' stellar population are useful but do not give enough discriminating power with respect to MW halo stars, the Pristine photometry is an ideal tool to separate the two populations (Fig. 7). This leads

to the rejection of 11 literature stars previously misclassified as Hercules members. Among those are the two most metal-rich stars in Hercules according to the literature, at [Fe/H] ~ -1.5 and [Fe/H] ~ -1.3, respectively (see Table 3), rejected because of their proper motion. This shows that Hercules' star-formation history is most likely shorter than previously thought.

Furthermore, we report the discovery of three new member stars, including one located at $9.5r_{\rm h}$ of the system, as well as three uncertain candidates likely to be MW contaminants. With this new sample, we find an inflated velocity dispersion ($8.0^{+1.4}_{-2.0}$ km s^{-1} km s^{-1}) and no statistically significant velocity gradient ($1.6^{+10.0}_{-3.8}$ km s^{-1} kpc^{-1}). In the unlikely event where at least one of the three uncertain stars is a member, the velocity gradient would be larger than any observed measurement or theoretical predictions for Hercules until now ($45.9^{+2.7}_{-2.6}$ km s^{-1} kpc^{-1}), which would point towards significant tidal interactions with the MW.

We simulated the CMD of a system with a similar luminosity as that of Hercules based on its best-fitting isochrone. To do so, stars following the best-fitting isochrone and luminosity function (LF) of Hercules were simulated, one by one with the typical SDSS photometric uncertainties and completeness taken into account. Similarly to Longeard et al. (2018), a star was simulated along the isochrone based on its probability computed from the relative number of stars at each luminosity given by the LF. Its luminosity is cumulated with the one of all the other stars. When the total luminosity reached the one of Hercules according to Muñoz et al. (2018), the process was stopped. Comparing the number of simulated RGB stars with the bona-fide, observed RGB members of Hercules shows that they should all have been identified. Therefore, if a significant amount of new RGB stars are discovered in the future, it would indeed mean that Hercules used to be more luminous, and therefore more massive.

Hercules has been over the years the subject of speculations as to its degree of tidal disruption, triggered first by its extremely elongated shape. The detection of an actual velocity gradient has been debated (Deason et al. 2012, Gregory et al. 2020), and *N*-body dynamical simulations of its orbit show that the satellite, if tidally disrupting, should exhibit a positive velocity gradient along its major axis, although its theoretical expected magnitude is also not clear (Küpper et al. 2017, Fu et al. 2019). Considering only the new AAT convincing Hercules members, this work does not show any evidence of a significant velocity gradient in Hercules, nor that it is part of a tidal stream. Finally, we also confirm the existence of an extremely large galactocentric star in the system, and more generally detected in some UFDs.

ACKNOWLEDGEMENTS

This work has been carried out thanks to the support of the Swiss National Science Foundation.

Based on observations obtained with MegaPrime/MegaCam, a joint project of CFHT and CEA/DAPNIA, at the Canada–France–Hawaii Telescope (CFHT) which is operated by the National Research Council (NRC) of Canada, the Institut National des Science de l'Univers of the Centre National de la Recherche Scientifique (CNRS) of France, and the University of Hawaii.

The authors thank the International Space Science Institute, Bern, Switzerland for providing financial support and meeting facilities to the international team Pristine.

GB acknowledges support from the Agencia Estatal de Investigación del Ministerio de Ciencia en Innovación (AEI-MICIN) and the European Regional Development Fund (ERDF) under Grant Number PID2020-118778GB-I00/10.13039/501100011033 and the AEI under Grant Number CEX2019-000920-S

NM gratefully acknowledges support from the French National Research Agency (ANR) funded project 'Pristine' (ANR-18-CE31-0017) along with funding from the European Research Council (ERC) under the European Unions Horizon 2020 research and innovation programme (Grant Agreement No. 834148).

This work has made use of data from the European Space Agency (ESA) mission *Gaia* (https://www.cosmos. esa.int/gaia), processed by the *Gaia* Data Processing and Analysis Consortium (DPAC, https://www.cosmos.esa. int/web/gaia/dpac/consortium). Funding for the DPAC was provided by national institutions, in particular the institutions participating in the *Gaia* Multilateral Agreement.

The Pan-STARRS1 Surveys and the PS1 public science archive have been made possible through contributions by the Institute for Astronomy, the University of Hawaii, the Pan-STARRS Project Office, the Max-Planck Society and its participating institutes, the Max Planck Institute for Astronomy, Heidelberg and the Max Planck Institute for Extraterrestrial Physics, Garching, The Johns Hopkins University, Durham University, the University of Edinburgh, the Queen's University Belfast, the Harvard-Smithsonian Centre for Astrophysics, the Las Cumbres Observatory Global Telescope Network Incorporated, the National Central University of Taiwan, the Space Telescope Science Institute, the National Aeronautics and Space Administration under Grant No. NNX08AR22G issued through the Planetary Science Division of the NASA Science Mission Directorate, the National Science Foundation Grant No. AST-1238877, the University of Maryland, Eotvos Lorand University (ELTE), the Los Alamos National Laboratory, and the Gordon and Betty Moore Foundation.

This project has received funding from the European Union's Horizon 2020 research and innovation programme under Grant Agreement No. 730890. This material reflects only the authors views and the Commission is not liable for any use that may be made of the information contained therein.

Based (in part) on data acquired at the Anglo-Australian Telescope, under OPTICON 2022A/041. We acknowledge the traditional custodians of the land on which the AAT stands, the Gamilaraay people, and pay our respects to elders past and present.

Funding for the Sloan Digital Sky Survey V was provided by the Alfred P. Sloan Foundation, the Heising-Simons Foundation, the National Science Foundation, and the Participating Institutions. SDSS acknowledges support and resources from the Centre for High-Performance Computing at the University of Utah. The SDSS web site is www.sdss.org.

SDSS is managed by the Astrophysical Research Consortium for the Participating Institutions of the SDSS Collaboration, including the Carnegie Institution for Science, Chilean National Time Allocation Committee (CNTAC) ratified researchers, the Gotham Participation Group, Harvard University, Heidelberg University, The Johns Hopkins University, L'Ecole polytechnique fédérale de Lausanne (EPFL), Leibniz-Institut für Astrophysik Potsdam (AIP), Max-Planck-Institut für Astronomie (MPIA Heidelberg), Max-Planck-Institut für Extraterrestrische Physik (MPE), Nanjing University, National Astronomical Observatories of China (NAOC), New Mexico State University, The Ohio State University, Pennsylvania State University, Smithsonian Astrophysical Observatory, Space Telescope Science Institute (STScI), the Stellar Astrophysics Participation Group, Universidad Nacional Autónoma de México, University of Arizona, University of Colorado Boulder, University of Illinois at Urbana-Champaign, University of Toronto, University of Utah, University of Virginia, Yale University, and Yunnan University.

We thank Ángel Rafael Lopez Sanchez who observed the AAT data used in this work.

We also thank Anke Arentsen for providing us the tools to more easily perform the data reduction.

DATA AVAILABILITY

The data underlying this article are available in the article.

REFERENCES

Adén D. et al., 2009a, A&A, 506, 1147
Adén D., Wilkinson M. I., Read J. I., Feltzing S., Koch A., Gilmore G. F., Grebel E. K., Lundström I., 2009b, ApJ, 706, L150
Aguado D. S. et al., 2019, MNRAS, 490, 2241
Arentsen A. et al., 2020, MNRAS, 496, 4964
Battaglia G., Helmi A., Tolstoy E., Irwin M., Hill V., Jablonka P., 2008a, ApJ, 681, L13
Battaglia G., Irwin M., Tolstoy E., Hill V., Helmi A., Letarte B., Jablonka P., 2008b, MNRAS, 383, 183
Battaglia G., Taibi S., Thomas G. F., Fritz T. K., 2022, A&A, 657, A54
Battaglia G., Tolstoy E., Helmi A., Irwin M., Parisi P., Hill V., Jablonka P., 2011, MNRAS, 411, 1013
Battaglia G. et al., 2006, A&A, 459, 423
Boulade O. et al., 2003, Instrument Design and Performance for Optical/Infrared Ground-based Telescopes, Vol. 4841, p. 72
Cannon R. D., 1997, in Kontizas E., Kontizas M., Morgan D. H., Vettolani G. P., eds, 2dF: the Two-Degree Field Facility on the AAT Wide-field spectroscopy, Vol. 212,p. 33
Carrera R., Pancino E., Gallart C., del Pino A., 2013, MNRAS, 434, 1681
Chambers K. C. et al., 2016, preprint (arXiv:1612.05560)
Chiti A. et al., 2021, Nat. Astron., 5, 392
Chiti A., Simon J. D., Frebel A., Pace A. B., Ji A. P., Li T. S., 2022, ApJ, 939, 41
Deason A. J., Belokurov V., Evans N. W., Watkins L. L., Fellhauer M., 2012, MNRAS, 425, L101
Deason A. J., Bose S., Fattahi A., Amorisco N. C., Hellwing W., Frenk C. S., 2022, MNRAS, 511, 4044
Dotter A., Chaboyer B., Jevremović D., Kostov V., Baron E., Ferguson J. W., 2008, ApJS, 178, 89
Errani R., Navarro J. F., Ibata R., Peñarrubia J., 2022, MNRAS, 511, 6001
Flores R. A., Primack J. R., 1994, ApJ, 427, L1
Fritz T. K., Carrera R., Battaglia G., Taibi S., 2019, A&A, 623, A129
Fu S. W., Simon J. D., Alarcón Jara A. G., 2019, ApJ, 883, 11
Gaia Collaboration 2022, A&A, 674, A1
Garling C. et al., 2018, ApJ, 852, 44
Gregory A. L. et al., 2020, MNRAS, 496, 1092
Hastings W. K., 1970, Biometrika, 57, 97
Johnson B. D. et al., 2020, ApJ, 900, 103
Kirby E. N., Cohen J. G., Guhathakurta P., Cheng L., Bullock J. S., Gallazzi A., 2013, ApJ, 779, 102
Kirby E. N., Cohen J. G., Simon J. D., Guhathakurta P., Thygesen A. O., Duggan G. E., 2017, ApJ, 838, 83
Koposov S. E. et al., 2011, ApJ, 736, 146
Kunkel W. E., Demers S., 1976, The Magellanic Plane, The Galaxy and the Local Group, 182, 241
Küpper A. H. W., Johnston K. V., Mieske S., Collins M. L. M., Tollerud E. J., 2017, ApJ, 834, 112
Lewis I. J. et al., 2002, MNRAS, 333, 279
Li T. S. et al., 2019, MNRAS, 490, 3508
Longeard N. et al., 2018, MNRAS, 480, 2609
Longeard N. et al., 2020, MNRAS, 491, 356
Longeard N. et al., 2021, MNRAS, 503, 2754
Longeard N. et al., 2022, MNRAS, 516, 2348
Lynden-Bell D., 1976, MNRAS, 174, 695
Martin N. F., Ibata R. A., Chapman S. C., Irwin M., Lewis G. F., 2007, MNRAS, 380, 281
Martin N. F., Jin S., 2010, ApJ, 721, 1333
McConnachie A. W., Venn K. A., 2020, Res. Notes Am. Astron. Soc., 4, 229
Minor Q. E., Pace A. B., Marshall J. L., Strigari L. E., 2019, MNRAS, 487, 2961
Moore B., 1994, Nature, 370, 629
Muñoz R. R., Côté P., Santana F. A., Geha M., Simon J. D., Oyarzún G. A., Stetson P. B., Djorgovski S. G., 2018, ApJ, 860, 66
Musella I. et al., 2012, ApJ, 756, 121
Oman K. A. et al., 2015, MNRAS, 452, 3650
Pace A. B. et al., 2020, MNRAS, 495, 3022
Pawlowski M. S., Oria P.-A., Taibi S., Famaey B., Ibata R., 2022, ApJ, 932, 70
Qi Y., Zivick P., Pace A. B., Riley A. H., Strigari L. E., 2022, MNRAS, 512, 5601
Robin A. C. et al., 2012, A&A, 543, A100
Sanati M., Jeanquartier F., Revaz Y., Jablonka P., 2023, A&A, 669, A94
Sestito F., Roediger J., Navarro J. F., Jensen J., Venn K. A., Smith S. E. T., Hayes C., McConnachie A. W., 2023a, MNRAS, 523, 123
Sestito F. et al., 2023b, preprint (arXiv:2301.13214)
Simon J. D., Geha M., 2007, ApJ, 670, 313
Starkenburg E. et al., 2010, A&A, 513, A34
Starkenburg E. et al., 2017, MNRAS, 471, 2587
Tarumi Y., Yoshida N., Frebel A., 2021, ApJ, 914, L10
The Dark Energy Survey Collaboration, 2005, preprint (arXiv:astro-ph/0510346)
Tolstoy E. et al., 2006, The Messenger, 123
Tolstoy E. et al., 2004, ApJ, 617, L119
Walker M. G. et al., 2016, ApJ, 819, 53
Waller F. et al., 2023, MNRAS, 519, 1349
Wolf J., Martinez G. D., Bullock J. S., Kaplinghat M., Geha M., Muñoz R. R., Simon J. D., Avedo F. F., 2010, MNRAS, 406, 1220
Yang Y., Hammer F., Jiao Y., Pawlowski M. S., 2022, MNRAS, 512, 4171
York D. G. et al., 2000, AJ, 120, 1579
Youakim K. et al., 2017, MNRAS, 472, 2963

APPENDIX A: MEMBERSHIP PROBABILITY TABLES FOR THE AAT SAMPLE

Table A1. All membership probabilities for Field 1 of the AAT sample. $\mathcal{P}_{\rm CMD}$ is for the CMD probability, $\mathcal{P}_{\rm v}$ for the probability from radial velocity alone, and $\mathcal{P}_{\rm PM}$ from the proper motion alone. Finally, $\mathcal{P}_{\rm Dyn}$ is the membership probability obtained from equation (3).

Name	$\mathcal{P}_{\rm CMD}$	$\mathcal{P}_{\rm v}$	$\mathcal{P}_{\rm PM}$	$\mathcal{P}_{\rm Dyn}$
Her 1005	0.00	0.00	0.00	0.00
Her 1017	0.07	0.00	0.00	0.00
Her 1023	0.74	0.00	0.00	0.00
Her 1074	0.01	0.00	1.00	0.00
Her 1	0.00	0.00	0.99	0.00
Her 250	0.77	0.02	0.00	0.00
Her 360	0.47	0.00	0.00	0.00
Her 395	0.02	0.00	0.00	0.00
Her 3	0.00	0.00	0.98	0.00
Her 409	0.09	0.00	0.00	0.00
Her 414	0.82	0.00	0.00	0.00
Her 442	0.01	0.13	0.00	0.00
Her 443	0.67	0.00	0.00	0.00
Her 452	0.61	0.00	0.00	0.00
Her 476	0.08	0.00	0.00	0.00
Her 508	0.00	0.00	0.00	0.00
Her 556	0.00	0.00	0.00	0.00
Her 599	0.76	0.00	0.00	0.00
Her 633	0.62	0.00	0.00	0.00
Her 658	0.65	0.00	0.00	0.00
Her 660	0.62	0.00	0.00	0.00
Her 662	0.79	0.00	0.00	0.00
Her 674	0.12	0.00	0.00	0.00
Her 675	0.68	0.00	0.00	0.00
Her 680	0.87	0.00	0.00	0.00
Her 684	0.91	0.00	0.00	0.00
Her 686	0.84	0.00	0.00	0.00
Her 693	0.10	0.00	0.00	0.00
Her 6	0.40	0.00	0.99	0.00
Her 707	0.68	0.00	0.70	0.00
Her 711	0.00	0.00	0.00	0.00
Her 712	0.01	0.00	0.00	0.00
Her 713	0.84	0.00	0.00	0.00
Her 719	0.58	0.00	0.00	0.00
Her 766	0.02	0.00	0.00	0.00
Her 770	0.83	0.00	0.93	0.00
Her 786	0.16	0.02	0.00	0.00
Her 787	0.91	0.00	0.00	0.00
Her 791	0.60	0.00	0.02	0.00
Her 793	0.63	0.00	0.00	0.00
Her 794	0.82	0.00	0.00	0.00
Her 795	0.78	0.00	0.00	0.00
Her 806	0.82	0.00	0.89	0.00
Her 807	0.67	0.00	0.00	0.00
Her 819	0.00	0.00	0.00	0.00
Her 829	0.70	0.00	0.00	0.00
Her 830	0.18	0.00	0.00	0.00
Her 831	0.79	0.00	0.00	0.00
Her 833	0.14	0.00	0.00	0.00
Her 835	0.80	0.00	0.00	0.00
Her 864	0.00	0.00	0.00	0.00
Her 865	0.56	0.00	0.00	0.00
Her 882	0.62	0.00	0.00	0.00
Her 897	0.34	0.00	0.00	0.00
Her 8	0.01	0.00	0.82	0.00
Her 928	0.34	0.00	0.00	0.00
Her 946	0.55	0.00	0.00	0.00
Her 951	0.87	0.00	0.00	0.00
Her 955	0.67	0.00	0.00	0.00
Her 962	0.59	0.00	0.00	0.00
Her 998	0.69	0.00	0.00	0.00

Table A2. Same table as the previous one for Field 2.

Name	$\mathcal{P}_{\rm CMD}$	$\mathcal{P}_{\rm v}$	$\mathcal{P}_{\rm PM}$	$\mathcal{P}_{\rm Dyn}$
Her 1	0.60	0.00	1.00	0.03
Her 10	0.09	0.79	0.79	0.88
Her 1028	0.54	0.91	0.00	0.00
Her 12	0.02	0.03	0.96	0.02
Her 128	0.11	0.00	0.97	0.00
Her 13	0.00	0.00	0.26	0.00
Her 159	0.76	0.00	0.98	0.00
Her 16	0.01	0.89	0.97	0.99
Her 17	0.04	0.77	0.65	0.74
Her 180	0.39	0.83	0.99	1.00
Her 193	0.62	0.00	—	0.00
Her 2	0.54	0.88	0.85	0.91
Her 20	0.01	0.88	0.94	0.94
Her 201	0.76	0.00	0.02	0.00
Her 202	0.86	0.01	0.00	0.00
Her 205	0.16	0.00	0.00	0.00
Her 218	0.00	0.20	0.00	0.00
Her 23	0.61	0.86	0.09	0.38
Her 235	0.76	0.00	0.01	0.00
Her 240	0.59	0.00	0.00	0.00
Her 255	0.21	0.00	0.00	0.00
Her 297	0.00	0.83	0.00	0.00
Her 298	0.83	0.88	0.00	0.00
Her 2	0.00	0.00	0.80	0.00
Her 3	0.74	0.94	0.99	1.00
Her 305	0.70	0.84	0.00	0.00
Her 309	0.00	0.86	0.00	0.00
Her 313	0.00	0.91	0.00	0.00
Her 321	0.88	0.22	0.08	0.02
Her 324	0.31	0.71	0.00	0.00
Her 325	0.74	0.00	0.00	0.00
Her 327	0.04	0.04	0.00	0.00
Her 328	0.23	0.00	0.00	0.00
Her 341	0.82	0.92	0.00	0.00
Her 397	0.19	0.84	0.00	0.00
Her 4	0.11	0.13	0.99	0.26
Her 401	0.66	0.00	0.00	0.00
Her 403	0.63	0.78	0.00	0.00
Her 405	0.83	0.00	0.00	0.00
Her 406	0.57	0.92	0.00	0.00
Her 410	0.84	0.90	0.00	0.00
Her 422	0.34	0.68	0.00	0.00
Her 432	0.82	0.91	0.00	0.00
Her 433	0.72	0.00	0.00	0.00
Her 434	0.90	0.00	0.00	0.00
Her 436	0.63	0.01	0.00	0.00
Her 446	0.01	0.75	0.00	0.00
Her 455	0.92	0.00	0.00	0.00
Her 464	0.64	0.82	0.96	0.98
Her 467	0.86	0.00	0.00	0.00
Her 468	0.11	0.05	0.00	0.00
Her 481	0.01	0.00	0.00	0.00
Her 483	0.79	0.00	0.00	0.00
Her 485	0.55	0.00	0.00	0.00
Her 487	0.68	0.00	0.00	0.00
Her 496	0.74	0.87	0.00	0.00
Her 497	0.53	0.74	0.91	0.82
Her 5	0.60	0.93	1.00	1.00
Her 513	0.44	0.00	0.00	0.00
Her 515	0.34	0.00	0.00	0.00
Her 525	0.75	0.68	0.00	0.00
Her 530	0.71	0.66	0.00	0.00
Her 561	0.00	0.57	0.00	0.00

Table A2 – *continued*

Name	$\mathcal{P}_{\rm CMD}$	$\mathcal{P}_{\rm v}$	$\mathcal{P}_{\rm PM}$	$\mathcal{P}_{\rm Dyn}$
Her 57	0.22	0.00	0.46	0.00
Her 570	0.01	0.85	0.00	0.00
Her 577	0.48	0.89	0.00	0.00
Her 578	0.42	0.85	0.00	0.00
Her 580	0.49	0.00	0.00	0.00
Her 596	0.06	0.00	0.00	0.00
Her 6	0.18	0.69	0.99	0.88
Her 603	0.81	0.52	0.00	0.00
Her 607	0.15	0.90	0.00	0.00
Her 614	0.80	0.00	0.00	0.00
Her 625	0.00	0.00	0.00	0.00
Her 626	0.81	0.84	0.00	0.00
Her 630	0.60	0.00	0.00	0.00
Her 631	0.01	0.00	0.00	0.00
Her 634	0.74	0.00	0.00	0.00
Her 636	0.62	0.78	0.00	0.00
Her 638	0.70	0.86	0.00	0.00
Her 639	0.17	0.01	0.68	0.01
Her 647	0.49	0.00	0.00	0.00
Her 671	0.18	0.06	0.73	0.07
Her 694	0.69	0.89	0.99	1.00
Her 698	0.25	0.06	0.00	0.00
Her 7	0.00	0.35	0.42	0.11
Her 719	0.83	0.05	0.00	0.00
Her 722	0.66	0.34	0.00	0.00
Her 733	0.31	0.00	0.00	0.00
Her 762	0.71	0.89	0.00	0.00
Her 786	0.00	0.92	0.00	0.00
Her 8	0.02	0.27	0.99	0.22
Her 861	0.68	0.29	0.00	0.00
Her 869	0.77	0.00	0.00	0.00
Her 890	0.70	0.00	0.00	0.00
Her 891	0.40	0.00	0.00	0.00
Her 893	0.36	0.00	0.00	0.00
Her 912	0.78	0.90	0.00	0.00
Her 92	0.41	0.00	0.98	0.00
Her 922	0.00	0.79	0.00	0.00
Her 925	0.71	0.00	0.00	0.00

This paper has been typeset from a TEX/LATEX file prepared by the author.